Turbulence in polymeric flows

A characterisation of Elasto-inertial turbulence and the Maximum drag reduction asymptote

by

Sarath Sankar Suresh

May, 2025

A thesis submitted to the
Graduate School
of the
Institute of Science and Technology Austria
in partial fulfillment of the requirements
for the degree of
Doctor of Philosophy

Committee in charge:

Robert Seiringer, Chair
Björn Hof
Alexander Morozov
Christian Wagner

Institute of Science and Technology Austria

The thesis of Sarath Sankar Suresh, titled *Turbulence in polymeric flows*, is approved by:

Supervisor: Prof. Björn Hof, ISTA, Klosterneuburg, Austria

Signature: ______________________________

Committee Member: Prof. Alexander Morozov, University of Edinburgh, Edinburgh, Germany

Signature: ______________________________

Committee Member: Prof. Christian Wagner, University of Saarland, Saarbrucken, Germany

Signature: ______________________________

Defense Chair: Prof. Robert Seiringer, ISTA, Klosterneuburg, Austria

Signature: ______________________________

Signed page is on file

ISTA Thesis, ISSN: 2663-337X

I hereby declare that this thesis is my own work and that it does not contain other people's work without this being so stated; this thesis does not contain my previous work without this being stated, and the bibliography contains all the literature that I used in writing the dissertation.

I accept full responsibility for the content and factual accuracy of this work, including the data and their analysis and presentation, and the text and citation of other work.

I declare that this is a true copy of my thesis, including any final revisions, as approved by my thesis committee, and that this thesis has not been submitted for a higher degree to any other university or institution.

I certify that any republication of materials presented in this thesis has been approved by the relevant publishers and co-authors.

Signature: ______________________

Sarath Sankar Suresh
May, 2025

Signed page is on file

Abstract

Flows of ordinary fluids such as water or air transition from laminar to turbulent motion as the velocity increases. This simple dependence of the flow state solely on inertia, does not apply to more complex substances such as polymeric- and biofluids which commonly have elastic as well as viscous properties. Here various different instabilities and turbulent states can arise at low and even vanishing inertia, while high inertia turbulence counterintuitively is suppressed and its drag strongly reduced. We here show in experiments of a viscoelastic model fluid that the phenomena observed at low and high inertia have a common origin and that the same dynamical state, elasto-inertial turbulence, persists across four orders of magnitude in Reynolds number, ranging from very low inertia, all the way to high inertia Maximum drag reduction (MDR) asymptote. We also explore the transitions from Newtonian turbulence to MDR, and specific cases of flow at high polymer concentrations, exploring the relationship between flow at these wide range of control parameters.

Acknowledgements

I have many people to thank for the successful completion of this thesis. First of all I'd like to thank my supervisor, Björn Hof, for the chance to work with him and the immense exposure it gave me in the subject. Thank you Björn for offering me a rather independent approach with my research, it allowed me to work in directions that I found interesting, and kept my curiosity alive.

I'd like to thank George Choueiri in helping me get into the experimental technicalities, and being a great mentor for my early years of PhD. Thank you Mukund for your enormous technical and moral support, and extremely helpful advice throughout my PhD. I'd like to thank Jose M Lopez, and Atul Varshney for our collaborations. Thanks also Shoaib Kamil, and Ziyin Lu for our collaborations, discussions, and help with many experiments that we performed in the lab together. I'm very grateful for ISTA machineshop, especially Astrit for helping me with fabrication and machining. I'd like to thank my colleagues and friends, Gökhan, Nischal, Michael, Baoying, Ankit and many current and older members of the group who have made my stay far more interesting than I could have asked for, and for our engaging after lunch discussions.

I could not have done this without my parents, who have always supported me in my efforts, and my sister for her support and company during this time. Thank you to Betti, Namitha, Sreyam and Andrea for their personal support in difficult times, your positivity and help is something I'm extremely grateful for.

This work was partially funded by the European Union's Horizon 2020 research and innovation programme under the Marie Skłodowska-Curie grant agreement No. 665385.

About the Author

Sarath Sankar Suresh completed his undergraduate degrees at Birla institute of Technology and Science, Pilani, India, double majoring with a B.E in Mechanical engineering and an MSc.(Hons.) in Physics. His main interests shifted to fluid dynamics during this time, after finishing a master's thesis at the Jawaharlal Nehru Centre for Advanced Scientific Research, before joining the Graduate schoool program at ISTA. His main research interests include polymer turbulence, a topic that has seen increasing development in recent years. During his tenure as a PhD student, Sarath has presented his work at various conferences, including the APS DFD in 2021 and 2022, the European Turbulence conference in 2023, and the European Fluid dynamics conference in 2024, and coauthored a paper in Proceedings of national academy of Sciences.

List of Collaborators and Publications

This paper contains three manuscripts preceded by an Introduction and an experimental methods chapter, followed by a conclusions chapter. The following three manuscripts are used, the first of which is published, and the latter two are under review and in preparation respectively. Please refer to beginning of chapters for declarations of reproduction.

Choueiri, G. H., Lopez, J. M., Varshney, A., Sankar, S., & Hof, B. (2021). Experimental observation of the origin and structure of elastoinertial turbulence. Proceedings of the National Academy of Sciences, 118(45), e2102350118. Reused in full, Chapter 3

S S. Suresh, B. Hof (2025) "Turbulence in viscoelastic fluids at low and high inertia". Unpublished manuscript, might reflect changes in time of publishing. Reused in full as 4

S Kamil, S S. Suresh, J. M. Lopez, B. Hof (2025) "Low Inertia limit of Elasto-inertial turbulence". Unpublished, in review in Physical Review Letters 5

.

Table of Contents

List of Figures

CHAPTER 1

Introduction

1.1 The transition to turbulence

Turbulence is a phenomenon that permeates nature, appearing across a vast range of scales from ocean currents to atmospheric flows, blood circulation to industrial processes. Despite its ubiquity, turbulence remains notoriously difficult to control and predict. Fundamentally, turbulent flows are governed by the Navier-Stokes equations, which describe the motion of Newtonian fluids.

The transition from laminar to turbulent flow is a central topic in fluid dynamics. The transition to turbulence is highly sensitive to the to external disturbances. A pioneering figure in the study of this transition was Osborne Reynolds, whose experiments in pipe flow laid the foundation for its modern understanding. Reynolds demonstrated that the onset of turbulence is associated with the appearance of eddies i.e chaotic, swirling motions . He introduced the a parameter, now called the Reynolds number (first named by Arnold Sommerfeld in 1909)[Rot90], which encapsulates the conditions under which flow transitions from smooth to chaotic. Reynolds observed that the onset of turbulence depended on the ratio of the bulk velocity (U) times the pipe diameter (D divided by the kinematic viscosity (ν). This dimensionless quantity is the measure of inertial forced to viscous forces in the flow. Hence in Newtonian flows, turbulence arises when inertial forces outweigh the viscous forces. However at the same time he could not provide an exact threshold for pipe flow, and found that this threshold greatly depended on the amount of finite amplitude disturbances present in the experiments. This issue aside Reynolds' findings allowed us to relate observations in different experiments by just knowing some basic physical parameters of the fluid and geometry: The density of the fluid, viscosity, characteristic length and velocity scales associated with the flow (For example, the bulk velocity and diameter, in case of flow in a pipe).

Turbulence is fully described by the Navier Stokes equations models the dynamics of turbulence [Bat00]in a Newtonian fluid. With enough resolution and computational power, all scales of turbulence can be fully resolved:

$$\frac{\partial \mathbf{u}}{\partial t} + (\mathbf{u}.\nabla)\mathbf{u} = -\frac{1}{\rho}\nabla P + \nu\nabla^2\mathbf{u} \tag{1.1}$$

with the incompressibility condition given as $\nabla.\mathbf{u} = 0$. Here $\mathbf{u}(\mathrm{m/s})$ is the velocity as a function of space and time, $P(\mathrm{Pa})$ is the pressure scale $t(\mathrm{s})$ is time, $\nu(\mathrm{m^2/s})$ is the kinematic viscosity, $\rho(\mathrm{kg/m^3})$ is the fluid density. The equation is nonlinear because of the second term on the left in Eq.1.1. The parameter Re arises out directly out of non-dimensionalising the N-S equations, as a reciprocal of the prefactor to the diffusion term in the equation.

The Newtonian laminar pipe flow is linearly stable, meaning that infinitesimal disturbances perturbing the flow get dampened. Consequently for pipe flows, it is possible to delay the natural transition by removing inlet disturbances in the experiment. In fact, Reynolds himself had noted this in his original experiments, where he could delay the transition to Re=13000.[Rey83][ABH23].This is also the reason the transition to Newtonian turbulence (NT) starts with the appearance of puffs, localised turbulent patches in an otherwise laminar flow. Recent studies have shown that whether the turbulence is sustained or not can be estimated from the lifetimes and the splitting probabilities of the puffs i.e. localised turbulent structures that occupy the transitional regime ($1700 < Re < 2400$). These quantities in turn depend on the Reynolds number.

The presence of polymers complicates matters further, both in case of dynamics with Newtonian like turbulence, and with respect to the transition problem to turbulence.

1.2 Polymer Drag reduction

Turbulence is ubiquitous in nature and practical in applications. While it is beneficial in many situations, as it leads to an increased heat transfer and mixing, turbulence at the same time drastically increases the fluid drag and causes substantial energy losses and increased pumping costs.

Moving viscous fluids takes up enormous amounts of energy, causing large energy costs in transport processes. It was discovered by Toms (1940) that the addition of long chain polymers causes a surprising reduction in the drag that occurs in the fluid as it is pumped[Tom48]. While allowing to considerably reduce pumping costs for example in oil pipelines, understanding this phenomenon and in particular the drag reduction limit, continues to pose a formidable challenge.

Early work on the mechanisms of drag reduction have broadly followed two methodologies. On the one hand the explanation of DR was made by comparing the temporal scales of the polymers, and that of the turbulence. This observation, as argued by Lumley in 1969[Lum69], posits that the the onset of drag reduction begins when the wall Weissenberg number (Wi) of the flow (the ratio of polymer relaxation time and the time scales at the wall) is of the order 1. The Lumley criterion proposes that the stretching of the polymers increases the effective viscosity at the wall, increases the buffer layer thickness, which in turn affects the Newtonian turbulent drag[Lum69].

On the other hand, Tabor and de Gennes came up with what is called the elastic theory for drag reduction[DG86][TDG86]. The main argument being that as the polymer travels through the flow and subject to the chaotic dynamics at the wall is in not one single state of stretch but a more complicated process of absorbing and releasing the energy from the flow as elastic energy. This stretching of the polymers then leads to taking away energy from the smaller scales of turbulence. This leads to a decrease in the kinetic energy at the smaller scales, cutting off the turbulent energy cascade, where larger eddies break up into smaller eddies.

The seminal work from Virk was one of the first comprehensive studies of this phenomenon of drag reduction[VMS70][Vir71][VSW97]. He discovered that the amount of drag reduction achieved asymptotically goes to a maximum limit, commonly known as the maximum drag reduction asymptote (MDR asymptote). Moreover Virk demonstrated that this drag reduction limit is independent of the kind of polymer used. Later studies introduced a further separation of the polymer drag reduction regime is further divided into two characteristic regions, later called Lower drag reduction (LDR) and Higher drag reduction (HDR) regime[WMH99], where HDR flows are termed as flows with roughly $> 40\%$ drag reduction. The mean velocity profiles differ significantly between these two regimes of flow. They conclude the differing mechanisms indicating a heavy role played by polymer stresses in the HDR regime. Near wall vortex structures have been found to be drastically reduced in highly drag reducing flows[WM08], consequently reducing the wall friction and modifying the mean flow profile in the process.

The above mentioned mechanistic interpretations of drag reduction rest on the assumption that the resulting non-Newtonian flows remain in a subdued state of inertial turbulence. This viewpoint specifically also includes the MDR asymptote. This limit is commonly interpreted as the marginal limit of inertial turbulence. Specifically, MDR has been associated in some studies with the basin boundary (i.e. the edge state) between Newtonian turbulence and laminar flow.[DTH23].

Early turbulence

The effect of polymers on transition to turbulence has long remained unclear and seemingly opposing observations can be found in the literature. Work from Draad et.al. found that for a pipe setup with a natural transition set to $Re = 60000$, addition of polymers caused transitions to happen earlier than one would expect, and in some cases it would delay the transition, suggesting that the transition to polymeric turbulence by increasing Reynolds numbers or shear rates is also non-trivial[DKN98]. Indeed, such instances of "early" transition were first found much earlier, as early as 1926, by Ostwald and Auerbach[OA26][DTH23]. This study hypothesised the turbulence results from the structure (ordering) of the polymers breaking apart and therefore proposed the name structural turbulence. Work from Ram and Tamir (1964) found that the structural turbulence can occur even at negligible Reynolds numbers[RT64]. Further experiments by Little et. al. suggested that the same mechanism that causes structural turbulence is the one that causes the drag reduction mechanism, suggesting a divorce from the theories of DR based on Newtonian flow modification[LW70]

1.3 Elasto-inertial turbulence

Samantha et al.[SDH$^+$13] in 2013 conducted a systematic analysis of transition scenarios from laminar to turbulent flow as a function of the concentration and Reynolds numbers. The experiments were performed both for a smooth and a perturbed inlet, to compare the transition properties with Newtonian turbulence. For low polymer concentrations, a delay in transition to Newtonian turbulence featuring the familiar turbulent puffs was reported. But at higher concentrations, the onset of turbulence occurred below the Newtonian transition Re. Unlike for the Newtonian fluids, no hysteresis was observed, i.e. the transition threshold did not depend on the inlet perturbation level. The lack of hysteresis in this new transition, along with the fact that the transition depended on Reynolds number and shear rate pointed to the existence of a new dynamical state, distinct from Newtonian turbulence, and one that could be triggered far below the Newtonian transition point. This state was termed Elasto-inertial turbulence (EIT). Samantha et.al in addition proposed that this state which is typically observed at low Reynolds number persists to high Reynolds number flows and that its responsible for a drag increase when compared to laminar flow. In particular, the authors suggested that the reason for polymers falling short of fully relaminarising Newtonian turbulence lies in the onset of EIT, which then is responsible for higher drag levels and the MDR.

Further experiments from Choueiri et.al. in 2018[CLH18a] exploited the circumstance that polymers delay the transition to Newtonian turbulence already significantly, before EIT is encountered. Consequently at moderate Reynolds numbers (3000), the authors could show that unlike proposed in earlier studies, an increase in polymer concentrations could surprisingly lead to a complete relaminarisation, hence surpassing the MDR asymptote. Moreover, the authors demonstrated that upon a further increase in polymer concentration, the laminar flow was destabilised at the onset of EIT, which caused an increase in drag and an approach to the MDR asymptote from below, from the laminar side.

With increasing polymers, turbulence was further suppressed, eventually leading to a reverse transition via slugs and puffs and the subsequent relaminarisation. The circumstance that EIT only arose subsequent to relaminarisation gave further evidence that the MDR limit is driven by EIT and to this being dynamically disconnected from NT, albeit this has been proven only for moderate Re of 3150.

The flow structures of EIT could only be resolved in experiments rather recently[CLV+21] using planar particle image velocimetry (PIV). Very close to the onset the flow was found to consist of alternate low and high speed regions that are organised in a noisy chevron like pattern, a structure that closely resembled a linear instability mode previously discovered by Garg et.al. in 2018[GCK+18]. This structure is associated with a centre mode instability. The onset at low dilutions scaled as $E(1-\beta)^{\frac{-3}{2}}$.The E in this case is the Elasticity number, which is defined as the ratio of the Wi and Re. β is a parameter based on the viscosity. (please refer to Chapter 2) Moreover the stability analysis predicts an upper limit for this instability to occur with increasing Elasticity. Experiments from the same group has found from microtubes that such a transition occurs following the scaling of $E(1-\beta)^{-0.5}$, by measuring the onset point using friction factor deviations.

The same centre mode instability has also been found for viscoelastic channel flows, and following the same relation as the viscoelastic pipe flow but extended to much lower inertia. The existence of such an instability on the channel has parallels to the pipe flow, but in this case the instability could be triggered at zero inertia conditions. More recently, Khalid et. al in 2021 found a subcritical route of transition route to EIT and found a continuous pathway to the zero inertia limit, and hence to purely elastic turbulence, suggesting an interplay between these two states[KSS21]. In their experiments in 2021, Choueiri et.al. further observed that the centre mode gives way to a wall mode as the Reynolds number was further increased[CLV+21].

Prior to these studies, Dubief et.al. in 2013 explored the mechanism of EIT in low to high Re (1000 to 6000)[DTS13]. They found that EIT was associated with sheets of inclined alternating high and low polymer extension. They proposed that, EIT arises from a nonlinear advection term associated with polymer conformation. Here the flow was dominated by near wall spanwise structures of isosurfaces of Q. The Q is the second invariant of the velocity gradient tensor, a quantity that can isolate rotational and extensional regions in a flow.

In a different line of work Dubief and coauthors carried out numerical investigation of two dimensional visoelastic channel flow and discovered a non linear traveling wave solution, dubbed the "arrow-head" that bifurcates from the center mode instability.[DPK+22][GCK+18][PDK20][BPK22]. The arrowhead gives rise to sub-critical instability branch that originates from the centre mode linear instability. These authors suggest that the state of EIT is organised around many invariant unstable solutions such as the arrow-head. While the arrowhead is stable at low Weissenberg numbers, it turns chaotic with increasing Wi.

A subcritical transition has also been reported by Lellep et.al. in three dimensional channel flows at low Re, where they identify a subcritical route to ET with the presence of the arrow head (which due to its appearance is also referred to as the narwhal)[LLM24]. This mode was triggered subcritically and was found to be directly linked to the centermode instability.

In an analogous weakly nonlinear study of pipe flow by Wan et. al. in 2021 [WSZ21], replicating the chevron structures in the linearly unstable mode. By scanning the parameter space, they also find the significance of increasing β (for dilute regimes, equivalent to decreasing the concentration). They predict that at high concentrations, or low values of β, the flow will transition supercritically, and subcritically for dilute solutions, or high values of β. They also find that the subcritical and the supercritical routes might not be easily distinguishable in laboratory experiment, due to threshold amplitudes remaining small, making a potential hysteresis undetectable from measurements. Choueiri (2021) [LCH19]confirms the same concerns, and pushes for more consideration of the non linear routes to transition. They also propose the shift from the center mode to the wall mode as arising from non-linear effects.

Another proposed route to EIT has been through the formation of Tollmien-Schlichting waves. The study observes that simulations of EIT display localized polymer stretch fluctuations resembling structures predicted by linear stability analyses, specifically Tollmien-Schlichting (TS) modes[SMW+19]. TS waves have first been associated with Newtonian turbulence. T-S waves are streamwise-traveling, two-dimensional disturbances that develop within the boundary layer of a fluid flow, and are important in understanding the formation of turbulence. These TS modes from the study from Shekar et.al. are characterized by critical layer structures in flow regions where the mean fluid velocity matches the wave speed[SMMG20]. They further propose that self-sustained nonlinear TS waves exhibit critical layers, leading to the formation of sheets of large polymer stretch. They propose that the dependence of EIT on solutions that look like TS modes might signal a connection with NT mechanisms, and as an explanation to the reason for a fixed MDR asymptote. A followup study found presence of this mode of unstable TS waves were not dynamically connected to the nonlinear TS wave branch in NT for the parameter ranges studied, indicating a viscoelastic driven effect. Another work from the same group also studied the effects of increasing Re and Wi. With increasing Re the weak stretching sheets of the strain field gave rise to much more elongated structures with stronger fluctuations. They link this mechanism to a coil stretch transition because of the Wi locally exceeding in value. In contrast with the flow at $Re = 3000$, at a higher $Re = 10000$ it was found that with increasing Wi Newtonian TS waves evolved continuously into EIT without the intermittent structures[SMMG21].

The study by Zhang et al. (2024) investigates further the transition to EIT[ZCW+24]. They find that the EIT requires a minimum streamwise domain length to sustain turbulence. When the channel length is below this critical size, the flow reverts to a laminar-like state, despite high Weissenberg numbers (Wi). By looking at the onset process for EIT, they hypothesise that the transition to EIT might involve the wall mode rather than the centre mode, because they observe the extended sheet like structures associated EIT, without going through the arrowhead states, indicating an existence of an MFU that sustains the EIT. In addition they describe the steady arrowhead (SAR) to exist when the domain lengths are too short, with increased Wi. They attribute this to the SAR being a state that appears due to insufficient channel lengths, and that for larger lengths, transition could be seen to EIT. They associate EIT to be strictly associated with the sheet like extension structures appearing along the wall, since the arrowheads are lacking of this feature. Studies were done at intermittent/transitional flows from SAR to EIT with increasing channel lengths, and it was observed that the near wall extensional structures that are associated with EIT arise without going through arrowhead, just like in the longer channel lengths, which would be indicative of EIT developing from a wall mode rather than a centre mode.

Although visoelastic linear instabilities in rectilinear geometries have only been found recently, for curvilinear flows a linear instability has been discovered much earlier. As shown by Larson and Shaqfeh Taylor-Couette flow undergoes a supercritical instability. A linear stability analysis of an Oldroyd-B fluid in this geometry showed the existence of elastic instability in this geometry, the onset depending on the Deborah number (An alternate formulation of Weissenberg number)[LSM90]. Further work from Groisman and Steinberg in 2000 shed further light into the nature of this instability that occurred in the presence of curvilinear streamlines[GS00][GS01]. They saw a sudden rise in fluctuations in a rotating flow, and could visualise it. The resulting turbulent flow persisted to vanishing inertia and was dubbed Elastic turbulence (ET). The underlying linear instability mechanism strictly requires curved streamlines and can hence cannot occur, at least as a linear instability in rectilinear flows, such as channel or pipe flows. [Ste21]. In an experimental study of viscoelastic channel flow, Pan et.al. propose that may occur subcritically, as a result of finite amplitude perturbations[PMWA13]. Such a non linear route to elastic turbulence was also predicted by Morozov and Saarlos in 2005[MvS05]. In their experiments, They triggered turbulence using a series of cylindrical obstacles situated close to the channel inlet, introducing curvilinear streamlines. For a threshold number of obstacles, the flow was observed to suddenly transition at critical Wi. Such experiments along with the numerical simulations has led to the question whether it is indeed the elastic instability that leads to EIT[PMWA13].

1.3.1 Potential links with MDR

As discussed above, MDR has previously been described as a marginal state of Newtonian turbulence, and not associated with elastic instabilities.

Notably, Xi and Graham(2010) suggested that MDR is related to the edge state of Newtonian turbulence and hence that the MDR is completely Newtonian in origin. These authors observe the flow existing in two configurations, named the active and hibernating regions of turbulence, which can be distinguished. As the name suggests, these regions correspond to regions of high and low turbulent activity respectively. They find that even in the Newtonian limit, the hibernating turbulence shows many characteristics of viscoelastic turbulence, namely long streaks and suppressed streamwise vortices. The active region consists of three-dimensionally varying structures, with strong streamwise vorticity, followed by regions of hibernating state, with suppressed streamwise vorticity and axially unchanging flow[XG10]. It was proposed that this period of the flow hibernating is the reason for the apparent reduced drag at MDR flow. Following from this, work from Xi and Bai (2016) worked on the edge state between laminar and NT states, concluding that this minimal state shows similarities to the hibernating turbulence[XB16].

A very different interpretation has been proposed by Choueiri et.al. from their work in 2018 and 2021. In their experiments they identify elongated velocity streaks MDR regime, that closely resemble the structures they observe at low Re EIT. Based on these observations and ton the earlier findings from Samanta et al. they argue that the flow state of MDR originates from EIT and is not a marginal state of NT. The strongest support for this proposition is the previously discussed observation that at moderate Re, the flow fully relaminarises with increasing polymer concentration, prior to the transition to EIT.[CLH18a][LCH19].

A study by Zhang et al from 2021 investigates the interplay between EIT and NT by employing DNS of viscoelastic turbulent channel flows using the Oldroyd-B model. They analyzed various flow regimes by varying Wi and Re IT to EIT and the resulting effects on drag reduction. The study demonstrated that EIT-related dynamics appear in drag reducing turbulence well before the flow reaches the maximum drag reduction (MDR) regime[ZZL$^+$21]. At moderate and high Reynolds numbers (Re), EIT and IT coexist both spatially and temporally. Initially, EIT emerges near the channel walls and gradually extends towards the center as elasticity increases. They argue that EIT like dynamics appears long before MDR state as the elasticity is increased. Zhang et. al. in a 2022 work also explore the same topic, finding high EIT dynamics at higher Elasticity numbers, indicating the MDR flow to be primarily associated with the EIT state[ZZW$^+$22].

Lu Zhu and Li Xi in their 2021 work show that the MDR state can exhibit characteristics of both IT and EIT, depending on the polymer properties, particularly the maximum extension length of the polymers. A critical value exists beyond which the flow dynamics transition from being IT-dominated to EIT-dominated, because of an additional effective elasticity due to the increased length. Through DNS of viscoelastic turbulent channel flows using the FENE-P model, they demonstrate that even as drag reduction approaches its asymptotic limit at MDR, the underlying flow dynamics continue to evolve without converging to a single, universal state, even though the friction does[ZX21].

Sid,et al.in 2018,investigated the contributions of EIT to flow at MDR state and its contribution to polymer-induced drag reduction in channel flows both 2D and 3D periodic channels. The study showed that the EIT dynamics tend to dominate over Newtonian dynamics in 2D flows, as one increases the Wi, and gets closer to MDR[STD18].

The Maximum drag reduction asymptote has remained an elusive state, owing to its asymptotic nature, and questions remain of its relationship to other flow states in the vicinity of the phase space. Only in recent years have we started getting a coherent structure of the mechanisms behind these flow states, and in spite of some parallels, opinions seem divided, and there's a need for more experimental studies to confirm many of these numerical studies.

1.4 Summary and Thesis objective

So far we have considered the story of viscoelastic turbulence, the various competing theories through history trying to explain it, the different transition mechanisms existing to these flow states. Initial research on this topic was focused on mechanistic descriptions based on Newtonian flows, and modification of Newtonian flow by polymers. In spite of some early research on early turbulence caused by polymers, the major work was focused on the Newtonian to MDR transition. Later research found out about low Re elastic turbulence, and pathways to such instabilities. The discovery of elasto-inertial turbulence brought up the question of the relationship between this novel state, with MDR, Elastic turbulence, and even Newtonian turbulence. Past few years in the research have turned out a lot of numerical and experimental work to support different possible transition scenarios, some linking EIT with MDR, with minimal interference from NT, and others indicating possibilities that MDR is an edge state of Newtonian turbulence, which gets stabilised by the presence of polymers.

In this work, we try to answer the question with regards to the relation between EIT and MDR. The second chapter presents the experimental methods used, and details on the performing of these experiments. The following three chapters contains the details of the results of the experiments. It has been indicated by many studies the important role that the polymer stretch plays in the dynamics of EIT. This is not a quantity that can be measured numerically from simulations, but not accessible via experiments. Visualisations in EIT until now have focused on 2-D measurements using planar particle image velocimetry. Despite the various routes to EIT proposed by the various studies in the recent years, the importance of gradient quantities like Q, and streamwise vorticities, and related quantities like polymer stretch that depend on shear can't be understated in studying these flows. We characterise the flow structures in three dimensions, allowing us to calculate quantities and components that might have been hidden from us before. Three dimensional visualisations of EIT have still not been obtained for elastoinertial turbulence. Such experiments allow us to look for well resolved data for long enough diameters, and compare it to existing flow states discussed in this chapter. Velocity statistics are also considered using spectral measurements from single point measurements in the flow, along with pressure measurements.

We present the first three dimensional experimental visualisations of polymer turbulence, at Reynolds numbers lower than the Newtonian transition point and hence at parameters where NT cannot arise, and those at higher Re in the maximum drag reduction limit. The study also explores the effects of the three parameters: polymer concentration, solvent viscosity, and flow rate, roughly equivalent to varying β, E and Wi/Re. The data that we get from this brings us a better understanding of the map of these flow instabilities. Further experiments are also done considering the NT to MDR transition in mind, to understand any possible relation to NT with MDR.

CHAPTER 2

Experimental methods

2.1 Experimental setup

2.1.1 Pipe setup and polymer preparation

For the experiments described here, the primary fluid is based on solutions of Polyacrylamide with a molecular weight of 18 Million (obtained from Polysciences). The polymers are dissolved in deionised water which increases the longevity of the solution, as tap water causes the polymers to degrade and lose elasticity with time. The flexible polymer is relatively prone to degradation from shearing, so the mixing of polymers is carried out in tall barrels of 50L capacity, rotating at a gentle pace between 10 and 20 rpm.

The major part of the experiments involving the visualisations and the calculations based on them are done on a 20mm pipe setup. A schematic of the setup can be seen in Figure 2.1. The flow was driven using a piston and a linear stage from Festo. The piston setup consists of a dual piston-cylinder arrangement each with an inner diameter of 11mm. A turbulent inlet introduces the flow into borosilicate glass pipes of 20mm inner diameter. Measurements were done in the forward direction, i.e. in the direction of pushing the piston. Two pressure sensors were connected along the length of the pipe, with common pressure ports, The Validyne DP15 pressure transducers were both equipped with diaphragms appropriate for the pressure drop across the corresponding pipe segment and for the flow rates studied.

Since each polymer solution is used for multiple runs, it is important that the rheological properties of the polymer do not change from one run to the next, for the sake of consistency. The protocol used to ensure this is as follows. After the piston cylinder is filled with the polymer solution, the piston is run at the maximum flow rate it is intended to be run at, with the pressure difference

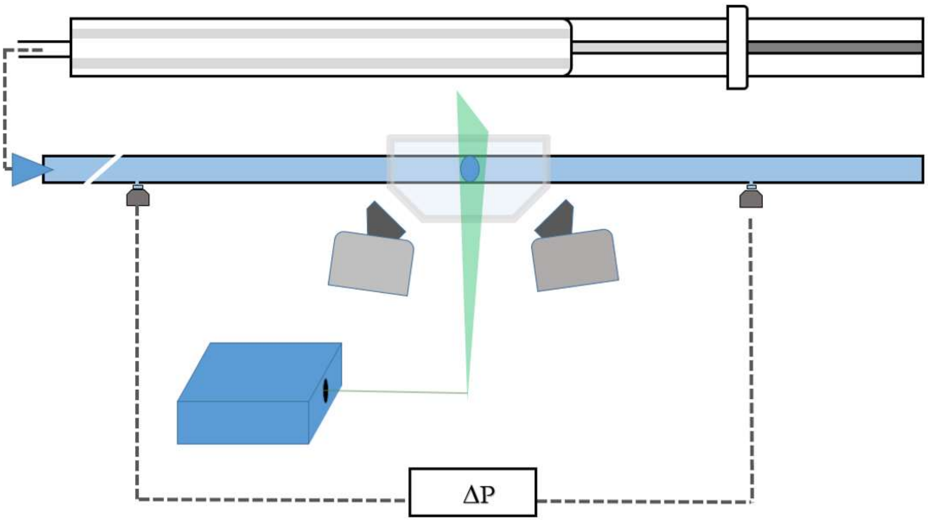

Figure 2.1: Schematic of experimental setup in 20mm pipe. The flow in this case is piston driven, with a dual piston cylinder setup with an inner diameter of $8mm$. The inlet is a natural turbulent inlet. Two synced cameras are placed for the stereo-PIV system, observing a laser sheet created by a pulse laser, running at the same frequency as the camera capture frequency

recorded. The pressure drop changes as the polymers get sheared, finally becoming stable. The actual experiments are done after the pressure drop has stabilised. This ensures that the rheological properties of the polymers stay consistent once the actual experiments are performed. Some additional experiments were conducted in a pipe with a 4mm diameter and the setup is described in Chapter 3.

2.1.2 Flow parameters and pressure measurements

In this section we cover details on pressure measurements, and basic flow properties in pipe flows. Let's consider a pipe flow with bulk velocity U, diameter of the pipe D, and a solution with dynamic viscosity μ. The walls are assumed to be smooth, and the flow is driven at a constant flow rate.

For Newtonian flows, the non dimensional parameter characterising the flow here is the Reynolds number, Re, defined as:

$$Re = \frac{\rho U D}{\mu} \tag{2.1}$$

For a smooth pipe, turbulence cannot sustain for $Re < 2040$, and the flow eventually always reverts to laminar. The laminar flow consists of a parabolic profile, that is to say, the mean velocity when plotted against the radial coordinate is exactly a parabola, with the maximum velocity occurring at the pipe center, and zero velocity at the walls according to the no-slip condition. The velocity at the center is exactly twice the bulk velocity. Turbulent flow on the other hand has a flatter average profile, which cannot be determined analytically, and moreover the shape of the profile depends on the Re.

A very useful way of characterising the flow is to measure the friction factor, which as the name suggests measures the friction in pipes, normalised by the bulk velocity. Consider a section of the pipe with pressure loss across that section as ΔP. We can calculate the friction factor from the Darcy Weissbach equation given as:

$$\frac{\Delta p}{L} = f_D \frac{\rho U^2}{2D} \tag{2.2}$$

where f_D is called the Darcy friction factor[Moo44]. A related quantity is the Fanning friction factor, which is exactly one fourth of the above friction factor. Both are widely used, and as long as one uses them consistently they give the same results. For laminar flow, the friction factor can be calculated analytically and scales as $f = \frac{16}{Re}$. For the Newtonian turbulent flow on the other hand, only empirical relations are known and here the scaling is given by the Prandtl Karman law:

$$f^{-0.5} = 2.\log(Re.f^{0.5}) + 0.4 \tag{2.3}$$

The friction factors for a non-Newtonian fluid at maximum drag reduction have been approximated by a similar relation by Virk[VMS70]

$$f^{-0.5} = 19.0 \log(Re f^{0.5}) - 32.4 \tag{2.4}$$

As shown in figure2.2 the friction factor corresponding to the MDR lies somewhere between the laminar and turbulent friction factors. The MDR asymptote is empirically derived, and starts to deviate from laminar flow only around $Re = 2000$

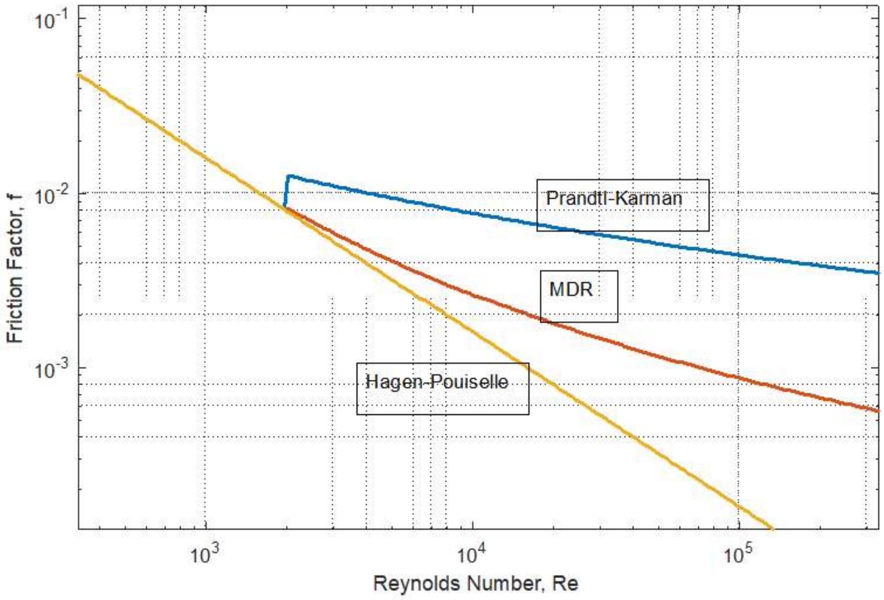

Figure 2.2: Friction factor plots representing laminar, turbulent and MDR flows

For calculating these friction factors, we first calibrate the DP15 Validyne pressure sensors based on either the laminar Hagen Pouiselle, or using the Prandl Karman relation, depending on the flow rates and pressure sensor ranges. Water is used as the working fluid. Care is taken that no bubbles enter the pipes connected to the pressure sensors, as this can change the zero-levels. Subsequently we measure the friction factors for the viscoelastic fluid and determine the friction factors. The Re in this case is calculated the same way as the Newtonian case, except that instead of the Newtonian viscosity, we use the viscosity corresponding to the wall shear rate.

2.1.3 Particle Image Velocimetry

Past experiments in the field have focused on resolving velocity structures in pipes using Particle Image Velocimetry (PIV). It involves suspending buoyant tracer particles in the flow, and illuminating a relevant section of the pipe with a laser. A (high speed) camera is placed orthogonal to the plane of the laser sheet, observing the position of the particles which trace the flow field. Consider two time instances of the flow close together. One observes that the particles move depending on the local velocity of the flow. If one divides the image into two grids, capturing the local flow, one can find the most likely displacement for each window by constructing a correlation function as follows:

$$C(\Delta x, \Delta y) = \sum_{x,y} f_1(x, y).f_2(x + \Delta x, y + \Delta y) \tag{2.5}$$

Where $f_1(x, y)$ and $f_2(x + \Delta x, y + \Delta y)$ are intensity functions in the first and second image respectively. The values of Δx and Δy where the function $C(\Delta x, \Delta y)$ takes a minimising value corresponds to the most likely displacement for the corresponding window.

In this manner, one can calculate the displacements and hence the velocities for each square on the grid. The cells in such a grid is called the correlation window, and these can be shaped to be more complicated to suit specific application purposes.

While PIV offers a great way to resolve structures in the flow, one is limited to components in the plane of the laser sheet in case of planar PIV. Resolving 3-dimensional velocity vectors is crucial to finding out the complete picture of the mechanisms of turbulent flow, as real world flows are three dimensional. To resolve the full velocity field in time and space would normally require volumetric techniques such as tomographic PIV where a volume is illuminated and recorded by multiple cameras. However for our purposes the recordings are limited to a cross section (see Fig. 2.1), and particle images are recorded by the two cameras. This was we get a three dimensional vector field on a two-dimensional plane of points.

Such a system consists of a laser illuminated plane being observed from two different perspectives. Looking at an object from multiple viewing angles allows for depth perception, and calculating the third velocity component which would have been missing in the case of a planar PIV system.

In a two camera PIV system, one has a couple of configurations that can be used for the visualisation.[RWS+18] The F-F (front-front) orientation, and F-B (front-back orientation.) The difference lies in whether the cameras are placed on the same side of the laser sheet being illuminated, or on the opposite side. In the current setup, a 20mm pipe was illuminated by a pulsed laser sheet in the $R - \theta$ plane, with two cameras placed in the F-B orientation. The scatter from a tracer particle is non-uniform in the front and back. Having the cameras on either sides of the laser sheet makes it easier to obtain equal signal to noise ratios in both cameras, which makes further correlations more

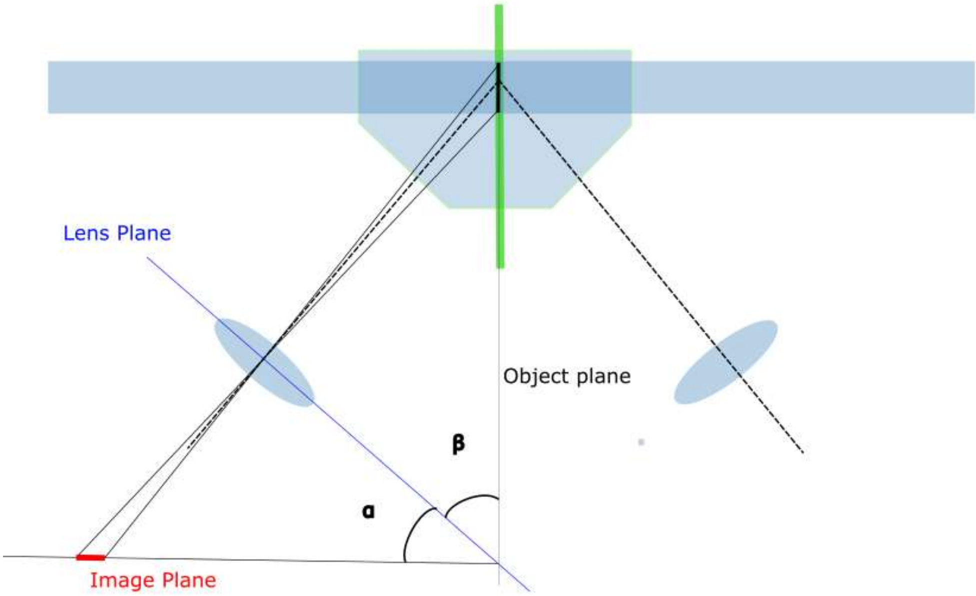

Figure 2.3: The Scheimpflug criterion for stereo-imaging. In a situation where the object plane, lens plane, and the image plane aren't parallel to each other, they need to intersect on a line, in order for the image to appear uniformly focused.

effective. This configuration has been used in several earlier pipe experiments and was originally suggested by Van Doorne and Westerweel (2007)[VDW07].

One major aspect to consider while using stereoscopic imaging is that the object plane, lens plane and the sensor plane are not parallel to each other. In planar PIV, adjusting the focus of the camera simply displaces the focus plane forward or backward, parallel to the object and the image plane. The thin lens approximation is the only equation controlling this scenario. In the case of stereo-imaging, where the sensor is not parallel to the illuminated laser sheet, things get more complex. Consider the image plane (IP), the object plane (OP) and the lens plane (LP). The adjustment of the magnification now not only displaces the IP, but also rotates it. For the image to be in focus, one needs the three planes to intersect along the line, and such an intersection is fulfilled by the Scheimpflug condition. In our case the magnification is close to 1, and the angles α and β as shown in the figure2.5 turn out to be roughly 45 degrees.The space between the lens and the camera are shielded by reflective aluminum tapes so as to avoid unnecessary light leaking into the sensors.

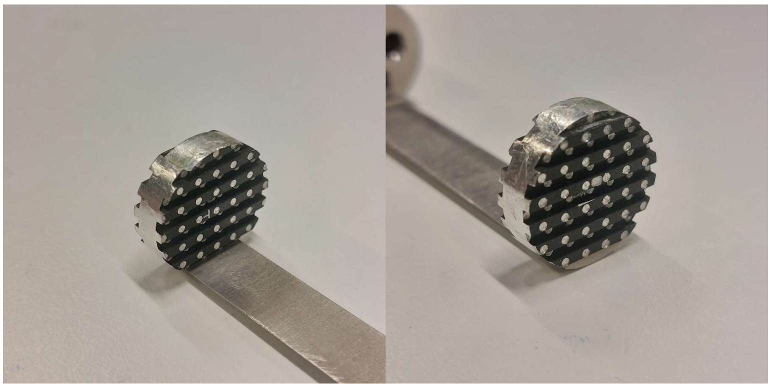

Figure 2.4: Calibration plate for 20mm pipe. The plate consists of four planes, two on each side. The dots make a grid with a grid length of $3mm$. The dots themselves have been precision machined to have a diameter of $1mm$. The plate along with the supporting plate is attached to a a base structure constructed from a combination of steel and plastic, which itself can be mounted onto long metal rods. The rods are used to push the whole structure into the pipe until it reaches the observation volume.

Because we have a complicated optical system, the calibration procedure for the Stereo-PIV system is more involved than for planar PIV. Since we have the cameras on either sides of the laser sheet, it was necessary to use a two-sided, four plane calibration plate to do the calibration. The plate consists of a precision machined steel disk, attached to a longer plastic holder which would allow it to be pushed through the pipe and placed at the appropriate position corresponding to the position of the laser sheet. The structure of the calibration disk is shown in Figure 2.4. Proprietary software from Lavision, Davis 8.4 is used for calibration using the plate. Further corrections and misalignment of the laser sheet with the plate that has been calibrated with, are done using a self calibration method, also included in the Davis 8.4 package.

The two cameras are synced using f-sync in a master-slave system, and a TTL signal from the master camera drives the second camera. The laser is a pulse laser, with the pulse width varying according to the flow rates. The cameras are indirectly synced with the pulsed laser, with the camera shutter being open for the majority duration of the cycle, and the image syncing happening as a result of the narrow pulse width of the laser, Care is taken between runs that

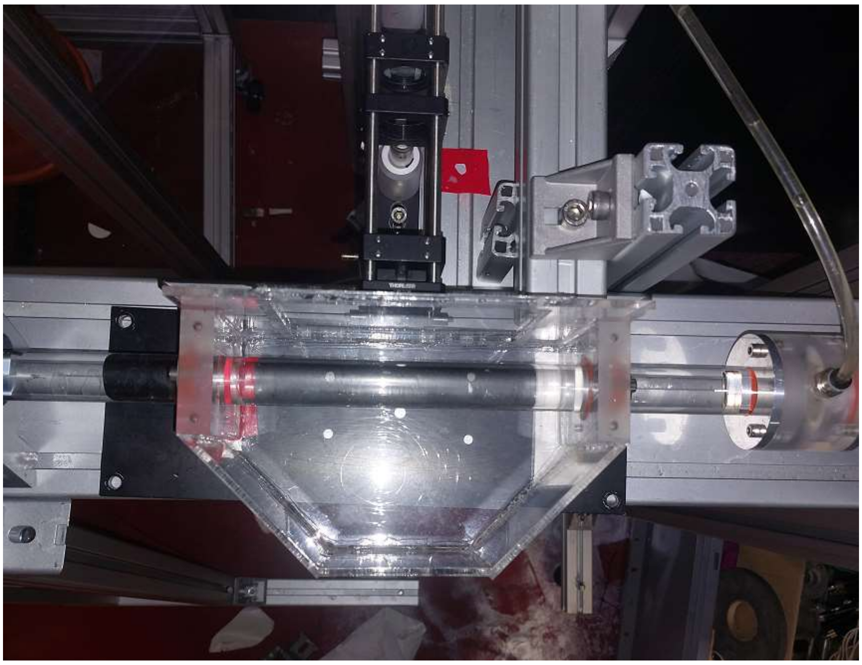

Figure 2.5: Index matching setup for the Stereo-PIV. The observation box is filled with the same solvent that constitutes the fluid inside the system. The sides are shaped such that they are parallel to the camera lens plane

the cameras have no drift between them. The laser beam itself is steered into a sheet using a system if concave mirrors, convex lenses, and a 45° Powell lens, which turns the beam into a sheet. The sheet is adjusted so as to maintain perpendicularity with the pipe, and is about 1.5mm thick. To correct for skewing due to changing refractive indices, the section of the pipe illuminated by the laser is placed inside an observation tank made out of PDMS, as shown in the , with faces perpendicular to the lens plane.

2.1.4 Proper orthogonal decomposition

Like all experimental measurements, PIV also is fraught with random uncorrelated noise. There are many classical methods of smoothing, for instance Gaussian smoothing, median based filters, and outlier removal algorithms. Naive smoothing methods such as these can cause a loss of crucial information, in addition to the removal of uncorrelated noise. This is because such methods do not capture the energies in the different length scales of the flow optimally. In contrast to this, Principal component analysis, or Proper orthogonal decomposition allows us to decompose the velocity fields into modes, and calculate a corresponding scalar value associated with each mode, which represents the energy contained in the said mode. This allows us to concentrate the bulk of

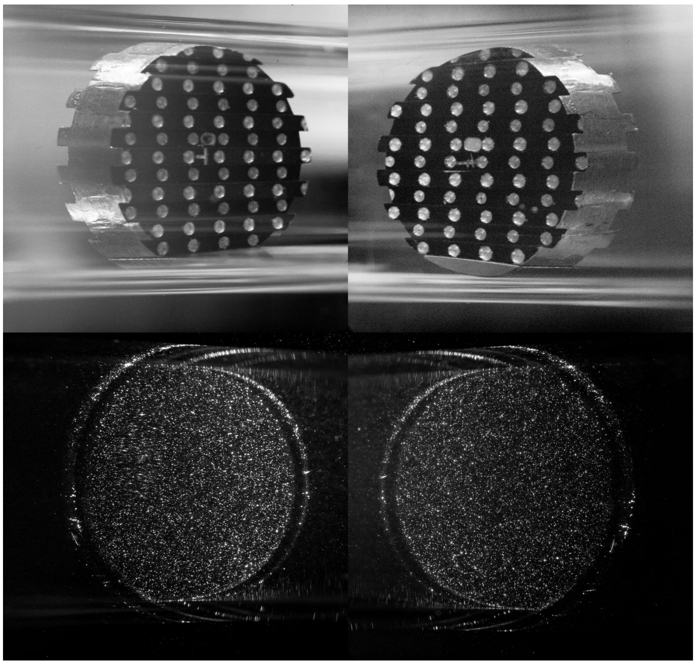

Figure 2.6: Two camera views of the calibration plate and the measurement volume with the particles in, for self calibration

the energy of the flow into a limited number of modes, and distributes the leftover uncorrelated noise into modes with insignificant energy[BV17].

This corresponds to decomposing the mean subtracted velocity field as:

$$u(x,t) = \Sigma_i a_i(t)\phi_i(x) \tag{2.6}$$

Where $a_i(t)$ are the time coefficients, and $< a_i(t).a_j^*(t) >= 0$, meaning that the modes are orthogonal. POD is a powerful tool to understand the dynamics of the flow, especially at onset of instabilities where certain unstable modes may prevail, or be dominant. In a developed turbulent flow, one can also identify all dominant modes, and combine a significant portion of these modes to reconstruct the flow, setting a cutoff energy,

In the current experiments, POD modes are summed until we have at least 95% of the energy within the flow field, and the residual vectors are mostly uncorrelated noise, allowing us to gain better access to derivative quantities.

2.1.5 Q structure calculations

We plot structures of the second invariant of the velocity gradient tensors, Q, from the reconstructed three dimensional velocity field that we obtain from stereo-PIV measurements. The values Q takes can be used to separate rotational and stretching flow. The combined values of the invariants of the tensor provides intricate information about the topology of the flow. Calculating these quantities helps us distinguish characteristics of flow topologies in EIT from that of Newtonian turbulence.

We define the velocity gradient tensor A_{ij} as

$$A_{ij} = \frac{\partial u_i}{\partial x_j} \tag{2.7}$$

This term can be split into the symmetric and anti-symmetric parts, which correspond to the strain-of-rate and rotation rate tensors respectively.

$$A_{ij} = S_{ij} + \Omega_{ij} \tag{2.8}$$

where

$$S_{ij} = \frac{\partial u_i}{\partial x_j} + \frac{\partial u_j}{\partial x_i} \tag{2.9}$$

$$\Omega_{ij} = \frac{\partial u_i}{\partial x_j} - \frac{\partial u_j}{\partial x_i} \tag{2.10}$$

By calculating the invariants of the velocity gradient tensor, we can determine the regions of various flow topologies in our area of interest. The characteristic equation for this tensor is given as

$$\lambda_i^3 + P\lambda_i^2 + Q\lambda_i + R = 0 \tag{2.11}$$

Where P, Q and R are the invariants of the velocity gradient tensor A_{ij}, and λ_i $(i = 1, 2, 3)$ are the eigenvalues of this tensor. For incompressible flows, $P = 0$. The second invariant of this tensor, Q, makes for a very good criterion for determining the boundaries of a "vortex"[HWM88], as the presence of vorticity itself does not imply the presence of a vortex. Here Q is defined as

$$Q = \frac{1}{2}\Big(\Omega_{ij}\Omega_{ij} - S_{ij}S_{ij}\Big) \tag{2.12}$$

We plot isovalues of positive and negative values of Q to differentiate between rotational (stable stretching/ unstable compressing) topologies from the ones that look like shearing (saddle node/ unstable node) topologies.

The third invariant of the velocity tensor when plotted with the second one gives more comprehensive view of the activity in the flow, but since these terms involve higher order powers of the velocity derivatives, and since there are limitations to accuracies of these terms derived from experiments, we limit ourselves to considering the second invariant.

In order to calculate the Q values, the velocity field is first reconstructed in 3D space, and all the individual derivatives are calculated. Because of the reconstruction being biased by the different streamwise velocities at different streamwise directions, correction factors are introduced proportional to the velocities, so that the gradients can be properly calculated.

2.2 Laser Doppler Velocimetry

In the previous section we discussed how stereo-PIV can help visualise flow fields in the bulk of the flow. While it is a robust way to determine aspects of the dynamics of the flow, it does have drawbacks, especially concerning resolutions. In such cases, it is very useful to employ another non-intrusive method, called Laser doppler Anemometry (LDA) or alternatively, laser Doppler Velocimetry (LDV). LDV is based on the Doppler effect, which occurs when the frequency of a wave changes due to the motion of the source or the observer relative to each other. In the context of LDV, this effect is observed in light scattered by particles moving within a fluid flow. We use silicon carbide powder averaging at around $3\mu m$ in size. The LDV system consists of a beam of a laser beam which is split in two by a beam splitter. Using a series of mirrors and lenses the beam is steered and calibrated, such that the beams cross over at a point, which is the observation point. The interference of the two beams causes a series of bright and dark fringe pattern. When a tracer particle passes through these fringes, they scatter the light back into the photodetector. The frequency of the scattered light, due to the Doppler effect is slightly changed according to the velocity of the particle that passes through it. In the experiments conducted we could obtain a frequency rate of up to 16000 Hz for the scattered signal, which was sufficient to calculate the Energy spectra of the flow.

One major challenge about calculating LDV spectra is the fact that the arrival times of the particles are not regular. This makes the calculation of the fourier transforms harder, and one has to modify the signal appropriately. There are multiple methods of doing this. One way for instance, is the Sample and hold[AY86], where the signal is held to be constant at the last detected value until the next burst updates this value. This method can lead to errors due to the introduction of a step-function like shape onto the actual signal, passing from one burst instance to the next. It can also cause spectral leakage, which wrongly attributes the energy of one energy scale to another.

In the current study, a method of arrival time quantisation with local normalisation as implemented by Nobach et.al is used[DKN18]. The arrival time quantisation uses weights based on inter-arrival times of the particles, and resamples the signal to create a quasi-equidistant signal. Instead of directly filling in the intervals with interpolated values, it replaces large gaps with zeros instead. Also a local normalisation algorithm is used for correcting the correlation estimate at each time lag. For more details on this technique, please refer to `http://ldvproc.nambis.de/programs/pyLDV.html` for further details on the procedure and python codes.

2.3 Rheology

2.3.1 Viscosity calculations

For the experiments presented in this thesis, solutions are prepared from a single batch of Polyacrylamide of a mean molecular weight of 18 Million Dalton. The long chain polymers are mixed in barrels at a low shear rate to reduce chances of degradation. The solutions are shear thinning, as opposed to Newtonian fluids, where the viscosity is found to be constant.

Shear thinning behaviour, or pseudoplasticity as it is alternatively called, is characterised by the measured viscosity changing as a function of the shear rate. At zero shear rate, the polymer molecules exist in a coiled state, effectively increasing the viscosity in the event of an applied shear. With increasing shear rate, the polymer molecules get stretched, aligning themselves in the direction of the flow, effectively decreasing the viscosity. There are a variety of models used to mathematically express such viscosities. The simplest of these is the power law model. In this case the viscosity is expressed as

$$\nu = K\dot{\gamma}^{n-1} \tag{2.13}$$

Where K is known as the consistency index, n is a dimensionless exponent, and $\dot{\gamma}$ is the shear rate.

As stated previously, for an incompressible Newtonian fluid pipe flow, the non dimensional constant defining the flow is the Reynolds number. The Reynolds number in this case also leads to the proper scaling of the friction factor. For a laminar Newtonian pipe flow, the $f = \frac{16}{Re}$ can be obtained analytically and is a well known solution. Non-newtonian viscosity relations makes the above equations obsolete, if one uses a constant viscosity in the equation for Reynolds number. If one uses the power law model, there is different but simple analytical solution as described by [DM59][MR55] which is given by

$$Re_g = \frac{U^{2-n} D^n \rho}{\dot{\gamma}} \tag{2.14}$$

The trouble with using this method is that although the power law model works well for intermediate shear rates for a variety of fluids, it fails at low and high shear rates, which are significant for the experiments presented in the current thesis. The power law model predicts an infinite viscosity at zero shear rate, and a infinitesimal viscosity and infinite shear rate, In reality, the viscosity profile of shear thinning fluids is observed to have two plateau regimes at high and low viscosities, with a transition region in between. The viscosity for shear thinning solutions like PAAm are modelled well by the Carreau yasuda model. This is given by the equation

$$\nu(\dot{\gamma}) = \nu_0 + (\nu_0 - \nu_\infty)(1 + \lambda \dot{\gamma}^a)^{\frac{n-1}{a}} \tag{2.15}$$

A straightforward approach to define the Reynolds number in this case is to replace the viscosity with the viscosity at the wall ν_w. [PW90]. The rheological characterisation of the viscosity is done on an Anton-Paar MCR102 rheometer. We use a cone and plate geometry to measure the viscosities. A small amount of the fluid is placed between two surfaces, a cone that rotates, and the base plate. One advantage of using this geometry is the fact that the shear rate that the flow is subjected to stays approximately the same throughout the span of the geometry. We measure the viscosities roughly from a shear rate of around $10s^{-1}$ to around 5000 or 1000^{-1}. Going to very high shear rates can cause instabilities and transitions to occur in the geometry, and hence an overestimation of viscosity. These portions are ignored, and removed from analysis. But since the shear rates achieved in the experiments are much less than the shear rates at which these transitions occur, it proves to not be a cause of concern.

The independent control of β, E, and Re is important, but also difficult in experiments. The parameter E in this case depends on the fluid used (for a fixed pipe diameter), while both β and Wi depend on the flow. The caluculation of Re is also more complicated, as now the Re is based on the viscosity corresponding to the wall shear rate. The same procedure goes for the parameter β, as this parameter can be calculated based on the viscosity at the wall shear rate. This makes presetting these parameters difficult in

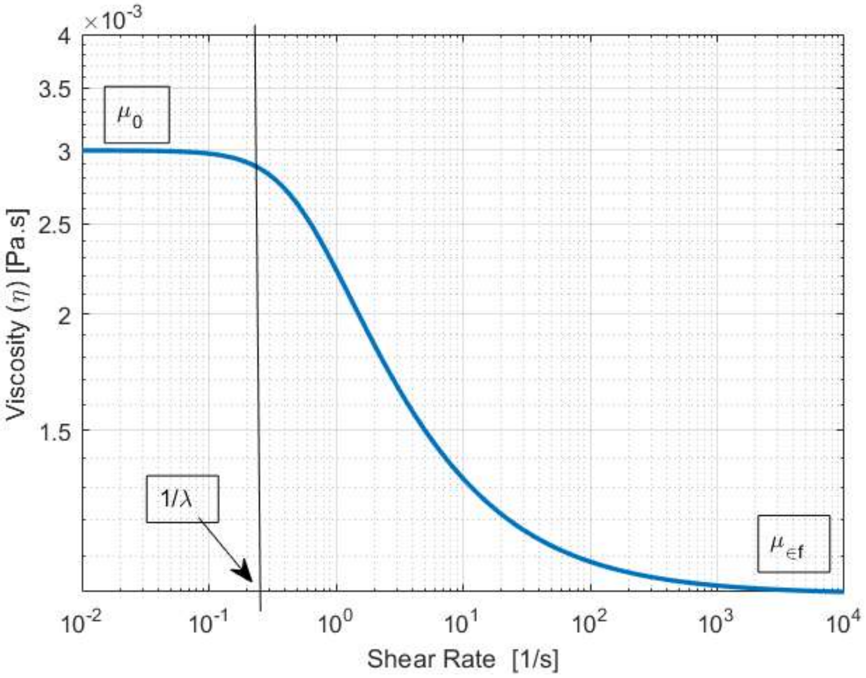

Figure 2.7: The Carreau-Yasuda model for shear thinning polymer solutions. It is a four parameter model, where the main parameters are μ_0, the zero-shear viscosity and μ_{inf}, the infinite-shear viscosity. The parameter a decides the smoothness of the transition regime between these two regimes, while λ determines at what shear rate this transition occurs. The parameter n determines the slope of this transitional regime

experiments, but they can be calculated These parameters were calculated a posteriori, from the parameters deduced from the PIV data.

It is important to have shear dependent viscosity data. The sweep experiment is done with a cone and plate tool attached at an Anton-Paar MCR102 rheometer. In order to calibrate the machine, an air check and motor adjustment is done before every run. The cone and plate geometries allows for uniform measurement shear rate across the flow. Since the present flow is viscoelastic, it does transition at high shear rates, showing an apparent increase in viscosity. But the shear rates at which such increases happen, for the current fluids that we've used seem to be much higher than the shear rates encountered in the experiments. The viscosities corresponding to these shear rates is then used for the calculation of the Reynolds number, and also the β.

Figure shows the shear rate based viscosities of some of the solutions used in the runs close to MDR. The shear rate dependent viscosities seem to not vary

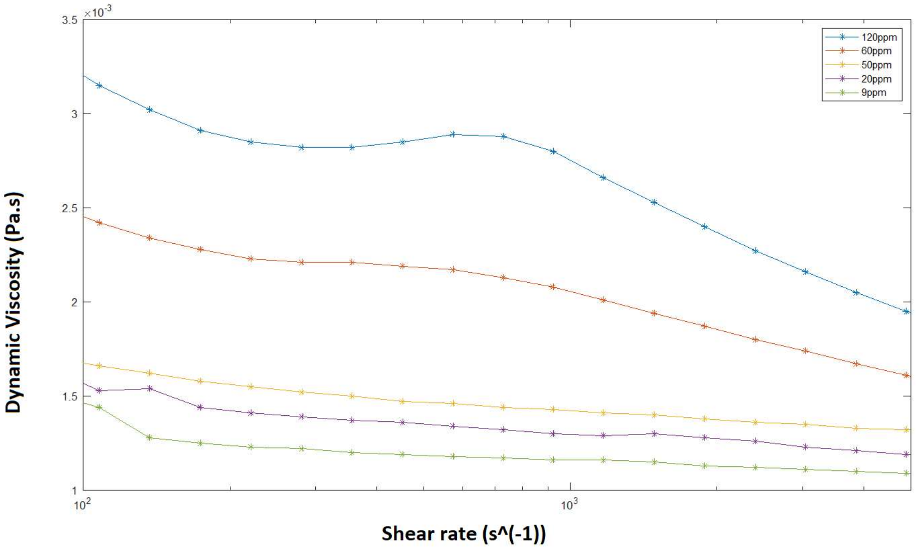

Figure 2.8: Shear based viscosity of various concentrations of PAAm solutions measured by shear rheometry

much in the very dilute regimes of polymer concentration, starting to rise only around the 60ppm mark.

2.3.2 Relaxation time calculations

Polymers exhibit a range of behaviors depending on their concentration in solution. In an unperturbed state devoid of shear flow, polymers typically assume a coiled conformation[Zim56]. The interaction and resultant properties of these polymer solutions can vary significantly with concentration.

In the dilute concentration regime, polymer molecules are well-separated with minimal interactions between them. This regime is effectively modeled using the Zimm model, which considers both hydrodynamic interactions and thermal motion[Zim56]. The Zimm model is expressed through equations that relate the relaxation time (τ) of the polymer to its molecular characteristics and the solvent viscosity:

$$\tau \propto \frac{\eta_s}{k_B T}\left(\frac{M}{N_A}\right)^{3\nu} \tag{2.16}$$

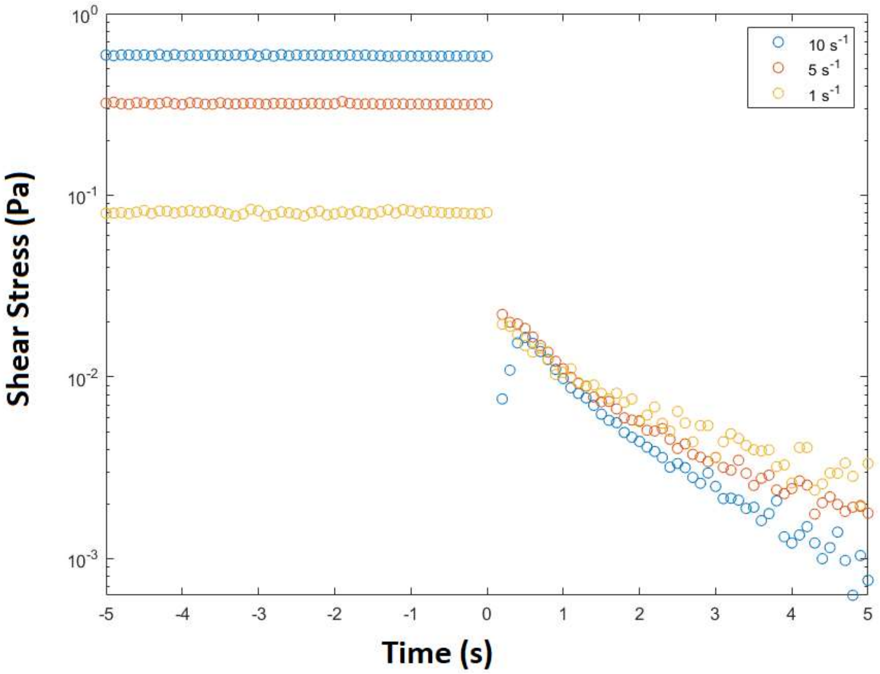

Figure 2.9: Cessation of shear flow using a cone and plate geometry. The working solution is a 20ppm solution in 80% glycerol water solution. The three curves correspond to three initial shear rates that the sample is subjected to

where η_s is the solvent viscosity, k_B is the Boltzmann constant, T is the temperature, M is the molecular weight, N_A is Avogadro's number, and ν is the Flory exponent.

As polymer concentration increases beyond the overlap concentration, the solution transitions into the semidilute regime. Here, the polymer chains begin to overlap, leading to an increased polymer contribution to viscosity and alterations in scaling laws:

$$\eta \propto c^{\frac{3\nu-1}{3\nu}} \tag{2.17}$$

where c is the polymer concentration.

In concentrated solutions and melts, polymers are highly entangled, characterizing this regime with strong inter-chain interactions.

Our experiments focused on a high molecular weight Polyacrylamide (18 million Da), a polymer extensively studied and well-documented by previous researchers, such as [LJS09]. We maintained polymer concentrations well within the dilute regime, significantly below the documented overlap concentrations.

The experimental procedure for determining relaxation times involves initially shearing the polymer solution at a constant rate, followed by an abrupt cessation of shear. The experiments were conducted in a viscous solvent composed of approximately 80% glycerol in water, aligning with the predictions of the Zimm model for dilute polymer solutions. According to the model, the relaxation time of the polymers scales proportionally with the solvent viscosity.

Following the cessation of shear, the polymer exhibits a typical viscoelastic relaxation, characterized by an exponential decay over extended periods. By fitting this decay with an exponential function, we derive the relaxation function, which is inversely related to the decay rate. To determine the intrinsic relaxation time of the polymer in water, we adjust for the viscosity ratio between the glycerol-water mixture and pure water. The relaxation times are found to be 50ms for 20ppm solution, and around 102 ms for the 100ppm solution, when adjusted for the solvent viscosity. The error bar for these values remain around 20 to 30ms.

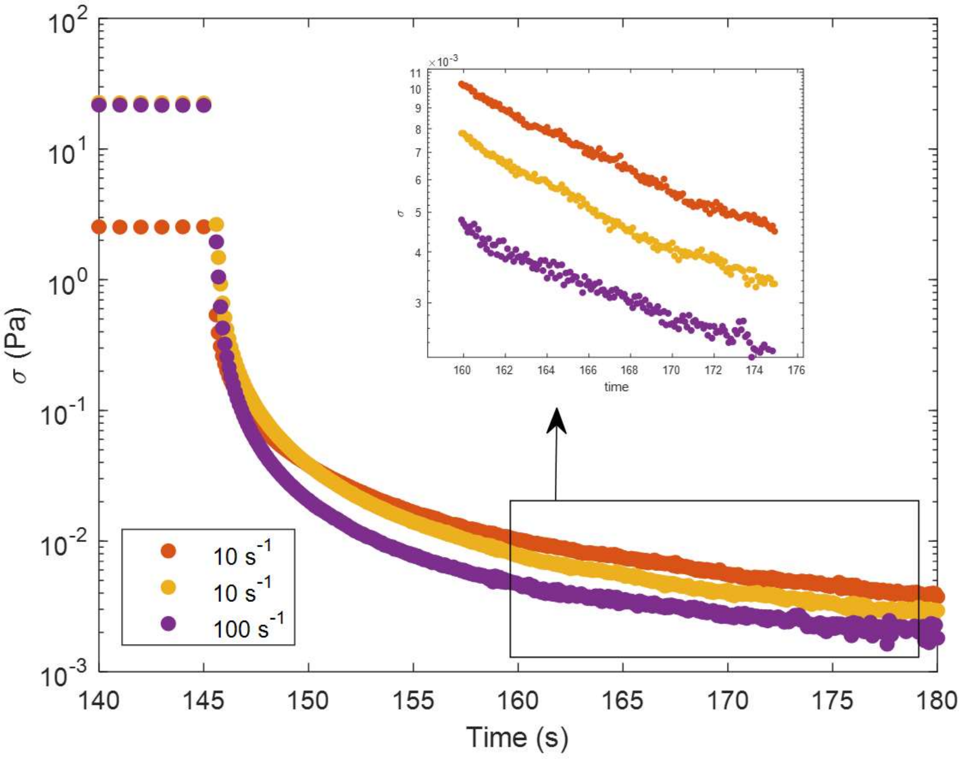

Figure 2.10: Stress relaxation after stopping of shear flow for a 100ppm solution of PAAm in 90% glycerol water mixture. The inset shows the exponential decay regime to find out the longest relaxation time. The relaxation time is obtained by fitting an exponential function on this regime, and finding the coefficient of decay with time. Since the relaxation time at the dilute regime is approximately linear in the solvent viscosity, this gives the relaxation time in water to be around 102 ms

CHAPTER 3

Experimental observation of the origin and structure of elastoinertial turbulence

This chapter reproduces the article G.H. Choueiri, J.M. Lopez, A. Varshney, S. Sankar, B. Hof, Experimental observation of the origin and structure of elastoinertial turbulence, Proc. Natl. Acad. Sci. U.S.A. 118 (45) e2102350118, `https://doi.org/10.1073/pnas.2102350118` (2021). published under the PNAS Author License (CC BY-NC-ND). © National Academy of Sciences. Reproduced with permission, under use for non-commercial purposes. The manuscript is copied as-is, with minor stylistic changes to adapt to the thesis format.

Author contributions: Rheological characterisation and analysis of data.

3.1 Abstract

Turbulence generally arises in shear flows if velocities and hence, inertial forces are sufficiently large. In striking contrast, viscoelastic fluids can exhibit disordered motion even at vanishing inertia. Intermediate between these cases, a state of chaotic motion, "elastoinertial turbulence" (EIT), has been observed in a narrow Reynolds number interval. We here determine the origin of EIT in experiments and show that characteristic EIT structures can be detected across an unexpectedly wide range of parameters. Close to onset, a pattern of chevron-shaped streaks emerges in qualitative agreement with linear and weakly nonlinear theory. However, in experiments, the dynamics remain weakly chaotic, and the instability can be traced to far lower Reynolds numbers than permitted by theory. For increasing inertia, the flow undergoes a transformation

to a wall mode composed of inclined near-wall streaks and shear layers. This mode persists to what is known as the "maximum drag reduction limit," and overall EIT is found to dominate viscoelastic flows across more than three orders of magnitude in Reynolds number.

3.2 Introduction

Many fluids in nature and applications, such as paints, polymer melts, or saliva, have viscous as well as elastic properties, and their flow dynamics fundamentally differ from that of Newtonian fluids. A standard example of such viscoelastic fluids is solutions of long-chain polymers, and here, surprisingly even very dilute solutions show a drastic suppression of turbulence and significantly lower drag levels[PLB08, WM08]. a phenomenon commonly exploited in pipeline flows to save pumping costs. In seeming contradiction to this stabilizing effect are observations at much lower Reynolds numbers (Re; the ratio of inertial to viscous forces), where polymers have the exact opposite effect; they initiate fluctuations and increase the flow's drag. The resulting chaotic motion was first detected in a narrow Reynolds number interval, $1000 \lessapprox Re \lessapprox 2000$, just below the onset of ordinary turbulence [RT64, LW70] and interpreted as a form of early turbulence. However, it was later shown [SDH+13] that the corresponding elasto-inertial instability can be traced into the polymer drag reduction regime at larger Re. The suggestion of a possible connection between these two seemingly opposing effects has sparked much recent interest in the phenomenon of elastoinertial turbulence (EIT)[DTS13][LCH19][SMW+19][GCK+18][CLH18b][CSD18][PDK20][CSD20]

It has additionally been speculated that EIT may be connected to purely "elastic turbulence," a fluctuating state driven by a linear elastic instability in the inertialess limit [GS00]. This instability requires curved streamlines [GS00**?** **?**] and is hence not to be expected in flows through smooth straight pipes. This does not, however, rule out the possibility that in planar flows, the instability may arise nonlinearly [MvS05], and this possibility has been supported by recent experiments [PMWA13, QSHA19].

Although EIT has first been observed in pipe experiments [RT64, LW70], information on the structure and nature of the resulting state is almost exclusively based on simulations using polymer models. Such simulations and theoretical considerations have suggested a range of possible transition scenarios. In direct numerical simulations (employing the Finitely Extensible Nonlinear Elastic-Peterlin [FENE-P] model), the characteristic features of EIT include near-wall vortical structures oriented perpendicular to the mean flow direction (i.e., spanwise direction) and elongated sheets of constant polymer stretch inclined with respect to the wall. In these simulations, the transition leading to this state is nonlinear (i.e., subcritical) and requires perturbations of finite amplitude [SDH$^+$13, DTS13, LCH19]. In another study, the aforementioned spanwise vortical structures were suggested to be linked to the well-known Tollmien–Schlichting (TS) instability that occurs in channel flow of Newtonian fluids at substantially larger Reynolds numbers. Again, here the transition would be subcritical but linked to TS waves [SMW$^+$19]. Yet other studies reported a linear instability that gives rise to chevron-shaped streaks [GCK$^+$18]. The latter proposed that this supercritical transition may be the starting point of a sequence of instabilities that eventually lead to EIT. Even more recently, FENE-P simulations of a simplified two-dimensional (2D) variant of EIT identified a subcritical scenario linked to the aforementioned linearly unstable mode [PDK20]

In the present study, we visualize the onset of EIT in experiments and show that the flow pattern is in excellent agreement with the unstable mode predicted by linear stability analysis [GCK$^+$18]. However, in experiments, fluctuations are already present close to onset, suggesting that nonlinear effects cannot be neglected. Moreover, for increasing elasticity number, the instability can be pushed to Re an order of magnitude below the parameter regime predicted by linear analysis. Although a quantitative comparison between experiments and computations remains challenging due to model limitations and difficulties in characterizing fluids, overall these observations suggest that the instability scenario is subcritical, an aspect that is also in line with the recent model study of EIT limited to two dimensions [PDK20]. For increasing Re on the other hand, the dominant flow structures adjust from a center to a wall mode, and fluctuation levels strongly increase. The resulting three-dimensional EIT flow pattern persists to the so-called “maximum drag reduction” (MDR) regime at much larger Re. Structural features of EIT can hence be detected across more than three decades in Re.

3.3 Results

Experiments were initially performed using a 50$\%$ water glycerol mixture as solvent and dissolving 600 parts per million (ppm) polyacrylamide with a molecular weight of $5 * 10^6$ Da (PAAm). The viscosity ratio (solvent/solution) of the fluid is $beta = 0.5$, while the elasticity number $E = \frac{8\lambda\nu}{D^2} = 3.4$ (where λ is the fluid's relaxation time, ν is its kinematic viscosity, and D is the pipe diameter). The SD of the pressure fluctuations recorded for increasing Reynolds numbers is plotted in Fig. 3.1. The fluctuation level is initially zero (when subtracting the sensor's background noise level), meaning that the flow is laminar, but it begins to grow at as the elastoinertial instability sets in. After the onset of instability, the fluctuation amplitude grows continuously with increasing Re, approximately in proportion to the square root of Re as indicated by the solid line. Nevertheless, given the small amplitudes and experimental uncertainties, other scaling relations cannot be ruled out.

Structural information is obtained from the velocity fields recorded in the pipe's central plane using particle image velocimetry (PIV). The instantaneous snapshots are assembled by applying Taylor's frozen-flow hypothesis, and the resulting flow structure is shown in Fig. 3.1 middle for for $Re \approx 100$. For visualization purposes the average cross-sectional velocity profile $\bar{U}$ is subtracted from the data and areas with velocities lower (higher) than the mean profile are shown in green (yellow). These low- and high-speed streaks alternate in the streamwise direction and show a tendency to form a chevron-type pattern. To compare these flow patterns with the unstable mode predicted by the linear stability theory, we repeated the analysis in ref. [GCK^{+}18]. The obtained results are in excellent agreement with those in [GCK^{+}18]. The least stable mode for $Re = 100$ is shown in the bottom panel of figure 3.1 (b). As seen, here, a chevron-type pattern consisting of alternating low- and high-speed streaks is also observed. Hence, the least stable mode can be detected in experiments, suggesting that the elastoinertial instability mechanism described in ref. [GCK^{+}18] is indeed central to the onset of EIT. However, while the stability analysis predicts a perfectly regular structure (resulting from a supercritical Hopf bifurcation), in our case the structure is not singly periodic, but fluctuations appear across a range of frequencies, suggesting weakly chaotic flow. Attempts to resolve the flow field closer to onset of instability for the same fluid were unsuccessful due to the vanishing fluctuation amplitude and lower signal to noise ratio. As the onset of EIT is approached, the fluctuation levels approach zero continuously. This is in contrast to Newtonian turbulence, where the internal dynamics of puffs have far larger amplitudes.

In order to probe if the elastoinertial instability persists to even lower Re, additional experiments were carried out for a 66% glycerol water solution, again adding 600 ppm of PAAm. The more viscous solution has a six times larger elasticity number (E = 20.8, β = 0.57). Indeed, for the 66% glycerol water mixture, fluctuations were detected at Re as low as 5, whereas at slightly lower Re 3, the flow was laminar. As shown in Fig. 3.1B, Top, at Re = 5, the flow again consists of alternating high- and low-speed streaks arranged in a chevron pattern. It is noteworthy that according to the linear analysis [GCK^{+}18], the instability can only be continued to Re 80 or so; this, however, does not rule out the possibility that the same mode may occur

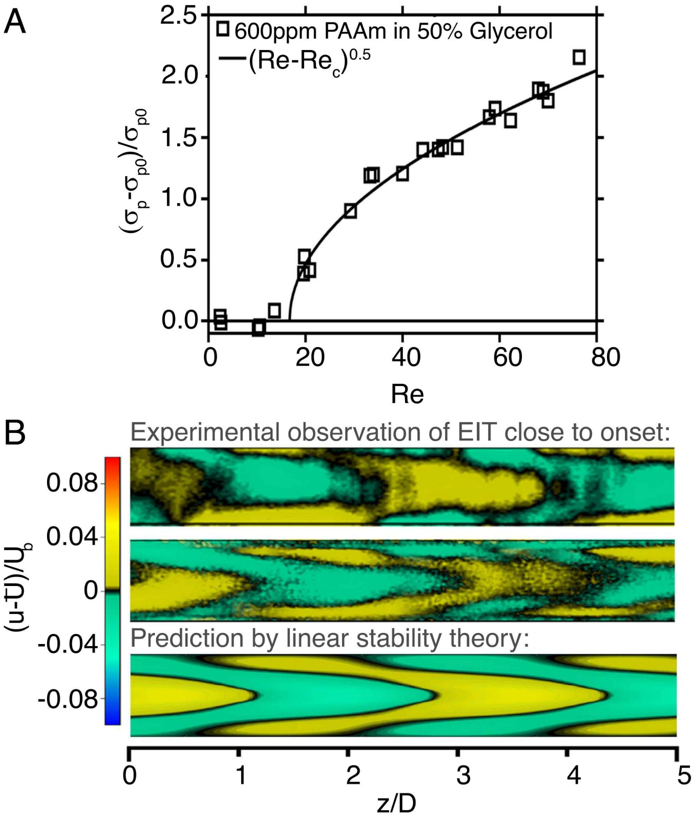

Figure 3.1: **Fluctuations level and flow structure near the onset of elasto-inertial instability**. Figure (a) shows the evolution of the pressure fluctuations amplitude with increasing Re close to the instability threshold for experiments using 600 ppm of PAAm dissolved in a 50% water glycerol mixture. The symbol σ_p denotes the standard deviation of the pressure fluctuations, $\sqrt{<p^2>}$, whereas σ_{p_0} indicates the standard deviation of the background noise level for the pressure sensor, $\sqrt{<p_0^2>}$. Figure (b) illustrates the flow's structural composition at Reynolds numbers near transition. The upper and middle panels show streamwise velocity fluctuations obtained from PIV measurements in a longitudinal cross section. The upper panel shows flow structures at $Re \approx 5$ and corresponds to an experiment using a 66% glycerol concentration ($\beta = 0.56$, $W_i = 96$), whereas the middle panel corresponds to $Re \approx 100$ in an experiment using a 50% glycerol concentration ($\beta = 0.56$, $W_i = 203$). The lower panel shows the most unstable mode in the linear stability analysis; the solution plotted was calculated for $Re = 100$,$W_i = 60$, $\beta = 0.9$, $n = 0$ and $k = 1$ (see SI for the definitions of these parameters). Flow direction is from right to left.

subcritically at even lower Re. Moreover, the flow pattern observed in our experiments at Re = 5 is again not perfectly periodic (unlike predicted by linear theory) but still weakly chaotic. Both these observations are consistent with a subcritical scenario where the minimum-amplitude threshold to trigger the instability, albeit finite, is low compared with the disturbance levels induced by typical experimental imperfections. In such a situation, EIT would arise automatically, even though in principle, the laminar state is linearly stable. The irregularities of the flow pattern observed are an indication that the state has undergone further bifurcations, and the resulting flow is chaotic and three-dimensional in nature.

We next investigate the further development of the flow pattern with increasing inertia (higher Re). In order to reach larger Re the solvent was changed to water again dissolving 600 ppm of PAAm and the resulting elasticity number $E = 0.08$. Owing to the reduced elasticity number, the onset of instability shifts to larger Re ($\gtrsim$ 200). Also for the 600ppm PAAm solution in water the transition appears to be continuous (inset of figure 3.2 (a)). With increasing Re the fluctuations level does not saturate but instead begins to increase faster and subsequently the scaling becomes closer to linear (figure 3.2 (a)). At the lowest Re $(= 300)$ where PIV measurements were carried out, the flow pattern still bears some resemblance to the chevron pattern (yellow and green isolevels shown in the top panel of figure 3.2 (b)), however in the near wall region higher amplitude streaks (red and blue isolevels) have appeared. While for the chevron patterns 3.2 (b)), fluctuation profiles show a central peak, the appearance of the large-amplitude streaks qualitatively alters the flow pattern to a wall mode as shown in Fig. 3.2B. With a further increase in Re, the near-wall streaks continue to increase in amplitude, while the chevron mode in the central region of the pipe disappears (the second panel in Fig. 3.2B). Inclined near-wall structures [often visualized in terms of polymer stretch [DTS13][SDH$^+$13] are a characteristic feature of EIT in numerical simulations; however, to date, inclined structures could not be confirmed in experiments.

Note that this mode change is equally found in the higher-viscosity solvents (50 and 66$\%$ glycerol concentrations) for Re sufficiently larger than those shown in Fig. 3.1B. With increasing shear levels, low- and high-speed streaks often appear in pairs that are approximately parallel, signifying strong shear layers at the respective interface (dashed black contours in Fig. 3.2B). Shear layers just like streaks are inclined with respect to the main flow direction and become more elongated with increasing Re, often extending multiple pipe diameters. We speculate that this mode change may result from a secondary instability. The generation of streak pairs has also been observed in a numerical study, albeit in the absence of walls, in homogeneous viscoelastic shear flow

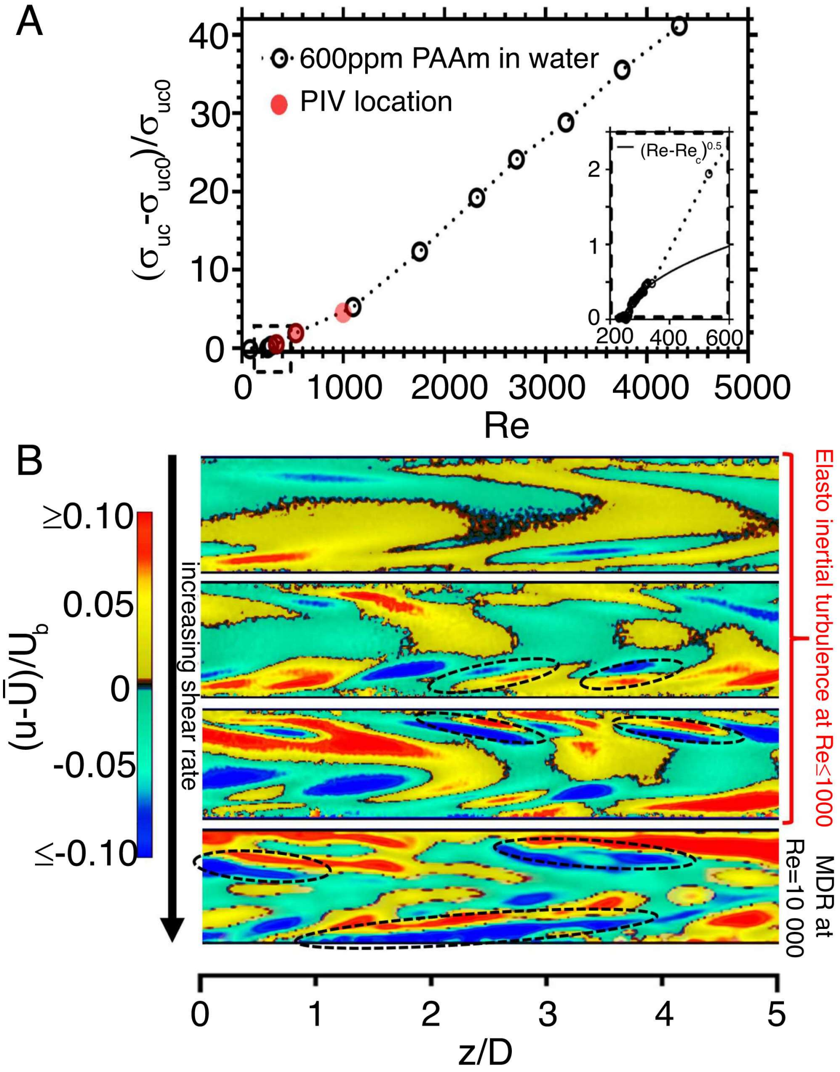

Figure 3.2: **Flow development far from the instability onset.** (a) Variation of the streamwise velocity fluctuations at the pipe center with increasing Re in experiments using 600 ppm of PAAm dissolved in water. The symbols σ_{u_c} and $\sigma_{u_{co}}$ denote the standard deviation of streamwise velocity fluctuations at the pipe centerline, $\sqrt{< u_c^2 >}$, and the standard deviation of the background noise level for the LDV system, $\sqrt{< u_{co}^2 >}$, respectively. The inset shows the deviation from the square root scaling. The red dots indicate the locations where the flow structures shown in panel (b) were measured. (b) PIV visualizations of streamwise velocity fluctuations. From top to bottom: $Re = 300$, $Re = 500$, $Re = 1000$ and $Re = 10{,}000$.

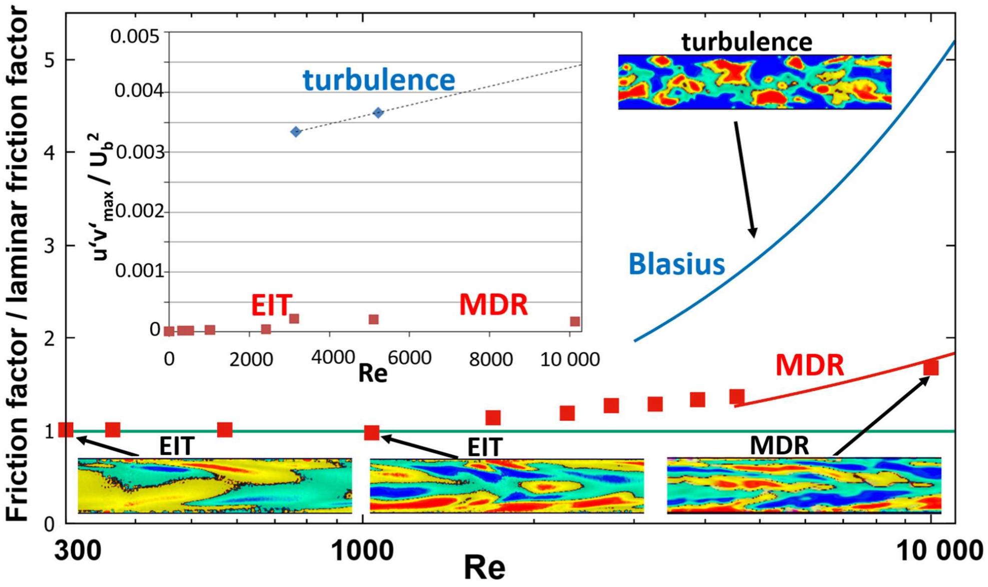

Figure 3.3: **Evolution of EIT as Re is increased within the polymer drag reduction regime.** The main figure shows the variation of the friction factor (f) as Re increases in experiments using water with 600 ppm of PAAm as working fluid. The inset shows profiles of mean streamwise velocity at several Re in the MDR regime. The superindex $+$ denotes inner normalization, i.e. velocity and length are scaled with the friction velocity, u_τ, and viscous length, δ_ν, respectively. As seen, the profiles are nearly invariant in this regime and fall within the 95% confidence interval on Virk's ultimate profile.

(20). As Re is further increased to $Re = 1000$(the third panel in Fig. 3.2B), there is surprisingly little change in the overall flow structure, and the wall mode continues to dominate the dynamics. Even for a 10-fold increase to (the fourth panel in Fig. 3.2B) and hence, a value that is well into the classical polymer drag reduction regime, the wall mode persists, and the flow's structural composition closely resembles that of EIT at, while it is clearly distinct from Newtonian turbulence (Fig. 3.3, Inset).

In addition to velocity measurements, the pressure drop was recorded as Re $=$ 10,000 was approached in order to determine fluid drag. The corresponding friction factors relative to the laminar level are shown in Fig. 3.3. At low Reynolds numbers, friction factors of EIT (red points) only marginally exceed the laminar friction. With increasing Re, deviations become notable, and the friction values smoothly approach what is known as the MDR or Virk's asymptote (red line). Regardless of the type of polymer, solvent, and relative concentration, Virk's asymptote sets a universal limit to the amount of drag reduction obtainable. Traditionally, MDR has been proposed as a residual, minimal level of ordinary turbulence, and a relation to the edge state of Newtonian turbulence has been suggested ([PLB08], [WM08], [XG10], [XG12]). This interpretation does not readily explain why polymers cannot reduce the drag beyond this level [reduction beyond MDR can be achieved in a narrow parameter regime only [CLH18a] but not at high Re]. As first suggested in ref. [SDH^{+}13], the MDR scaling may instead be caused by the EIT instability (i.e., although polymers can largely suppress ordinary Newtonian-type turbulence, eventually when shear levels are sufficiently large, the elastoinertial instability necessarily must arise, inhibiting laminarization).

It is noteworthy that in the present study as the high-inertia regime is approached, the MDR friction scaling monotonically arises from low Reynolds number EIT. Structurally, MDR and EIT are equally composed of elongated inclined streaks and shear layers. In contrast, streaks in Newtonian turbulence are shorter and less coherent (Fig. 3.3). In addition to the structural composition and the skin friction levels, the Reynolds shear stress also (Fig. 3.3, Inset) smoothly links low–Reynolds number EIT and high–Reynolds number MDR, whereas Newtonian turbulence levels are an order of magnitude larger[WMH99]. The same holds for velocity fluctuations (Fig. 3.2A). It should be taken into account that unlike EIT, Newtonian turbulence necessarily arises via spatially localized structures (puffs and slugs) and spatiotemporal intermittency. These localized structures require finite-amplitude fluctuation and friction levels and hence, do not smoothly develop from low levels. EIT, on the other hand, is never spatially localized but always space filling, a feature that persists during its development to high Re and MDR.

The state space considered in this work, although broad in terms of Reynolds and elasticity numbers, represents only a subset of possible parameters. For example, the dependence on polymer concentration, Weissenberg number, viscosity ratio, polymer chain length, etc. have not been explored and are left for future studies. In particular, it will be interesting to explore if in a different part of parameter space, the chevron pattern at onset may settle to the exact axisymmetric (i.e., 2D) chevron mode, as predicted by linear analysis.

In summary, we have shown in experiments that EIT arises from a center mode chevron pattern in qualitative agreement with linear stability theory [GCK^{+}18]. From theoretical considerations, it is evident that this mode requires finite inertia[GCK^{+}18]. This relevance of inertia suggests that EIT is distinct from purely elastic turbulence, although a more recent theoretical study [KSS21] indicates a connection between the two instability mechanisms at least for a very narrow parameter window. On the other hand, the transition is considerably more complex than the instability suggested by linear analysis [GCK+18]. Although fluctuation amplitudes appear to increase continuously and at first sight seem to support a linear instability and a supercritical scenario, as shown in Fig. 3.4A the onset of EIT can be pushed to Reynolds numbers more than an order of magnitude lower than permitted by the linear theory. Moreover, linear theory predicts a nonmonotonic dependence of the critical Reynolds number at which the instability occurs; in experiments, we find that the threshold decreases monotonically. Although given the difficulties in modeling and characterizing polymer solutions, a quantitative comparison between experiments and theory remains challenging, the monotonic decrease to very low Reynolds numbers strongly supports a subcritical scenario. This subcritical nature is equally supported by the chaotic three-dimensional motion detected even close to onset. On the other hand, experiments cannot strictly rule out that upon an even closer approach to the critical point, the flow pattern may yet settle to the unperturbed (supercritical) mode.

In order to allow quantitative comparison with experiments, future theories must take nonlinear effects and the three-dimensional nature of EIT in experiments into account. Regarding the latter, shortcomings of 2D simulations have also been pointed out in a recent numerical study [ZX20]. With respect to the former, a theoretical (Riemannian) framework enabling a (weakly) nonlinear approach has been introduced recently [HMZG18, HGZ19]. Subsequent to the present study, weakly nonlinear analyses have been carried out for pipe [WSZ21] and channel flows and established the robustness of the chevron mode (figure 8A in ref. [WSZ21]). These findings retrospectively rationalize the mode's persistence to the weakly chaotic regime reported in the present experiments. Moreover, both theoretical studies tested our suggestion that a subcritical route may not be readily distinguishable from a supercritical one under realistic experimental conditions if threshold amplitudes, albeit finite, remain small. As shown by ref. [BPK22], even well into the subcritical regime, threshold amplitude indeed remains small. Looking beyond the regime traceable by stability analysis, our experimental observations suggest that nonlinear effects are in particular relevant for the flow's subsequent transformation from a center (Fig. 3.4B, red points) to a wall mode (blue points). It is this latter flow transition that gives rise to the near-wall inclined structures characteristic for EIT [SDH+13] and to a more rapid increase of fluctuation levels. This structural change occurs at Re of order 102 and hence, far below the inertia levels required for Newtonian-type turbulence. The resulting flow pattern

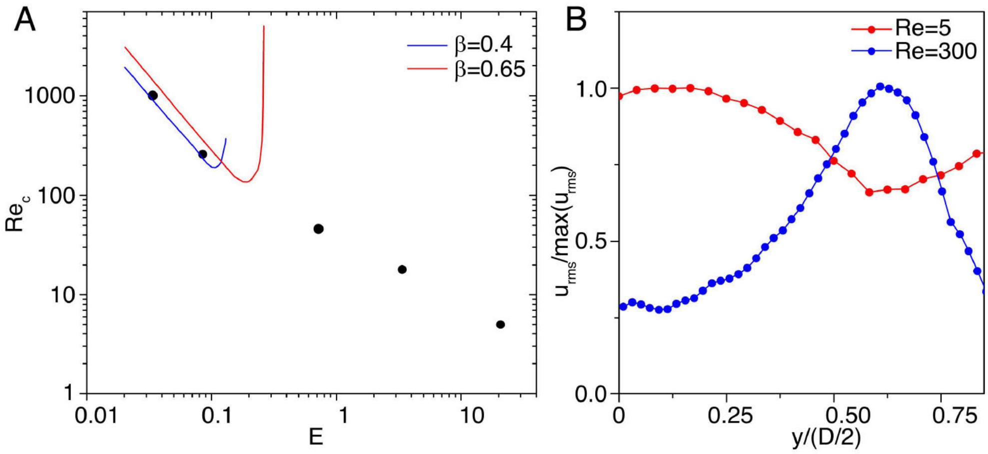

Figure 3.4: Onset of EIT. (A) Elasticity number dependence of the transition threshold. In experiments (black circles), the transition Reynolds number for the onset of EIT decreases monotonically with the elasticity number. While at low elasticity numbers, the experimental data are in good agreement with the threshold predicted by linear stability theory (9), linear analysis predicts a nonmonotonic dependence that is not found in experiments. At high elasticity numbers, the onset of EIT occurs at Re more than an order of magnitude below the theoretical prediction. (B) Change from a center to a wall mode with increasing Re. For the chevron pattern EIT exhibits close to onset (Fig. 3.1A), the rms of the streamwise velocity fluctuations has a peak close to the pipe center (red data points, Re = 5, E = 20.8). Sufficiently far above onset, the central peak disappears, and the highest fluctuations are found closer to the wall (i.e., at the location of the inclined streaks and shear layers [the second panel in Fig. 3.2B]; Re = 300, E = 0.08).

remains qualitatively unchanged with increasing Re, demonstrating that EIT is active in the MDR limit and hence, inhibits flow laminarization even if polymers ultimately were to completely eradicate ordinary turbulence.

3.4 Methods

Experiments are carried out in a 1.1-m-long smooth glass pipe with an inner diameter D = 4 mm. A smooth inlet ensures that the gravity-driven water flow remains laminar to Re greater than 5,000. Starting from 150D downstream of the inlet, the pressure drop is measured over a pipe length of 75D using a differential pressure sensor (DP15; Validyne Engineering). Directly downstream, an identical sensor is used to measure pressure fluctuations over a pipe length of 4D. A planar PIV system (LaVision GmbH), located 250D downstream of the pipe inlet, is employed to monitor the velocity field in a radial–axial cross-section. At the same location and positioned at the pipe center, a laser Doppler velocimetry (LDV) system (Powersight; TSI GmbH) is used to measure the axial velocity component.

The working fluid is a 600-ppm (by weight) PAAm (lot 685910; Polysciences, Inc.) solution in either water or water glycerol mixtures (50 and 66$\%$glycerol). The addition of glycerol effectively increases the viscosity of the Newtonian solvent and allows us to investigate flows at low Reynolds numbers while keeping the shear rates and hence, elastic forces (or more precisely, the Weissenberg number) high. The chosen polymer concentration approaches the upper end of the dilute limit (estimated from the measure of intrinsic viscosity to be 700 ppm).

3.5 Supplementary information

3.5.1 Rheological characterization of the polymers

The shear viscosity and longest relaxation times (λ) of the dilute polymer solutions used in our experiments are measured at 20$\circ$C in a commercial rheometer (MCR102, Anton Paar) with cone-plate geometry; cone angle $0.5\circ$ and cone diameter 60 mm. For the measurement of (λ), a polymer solution of concentration 600 ppm (PAAm, Molecular weight=5 MDa) was prepared in a viscous solvent of 80% glycerol and 20% water by weight. Shear-rate dependent viscosities of the polymer solutions used in the experiments, i.e. 600 ppm PAAm in water and water-glycerol mixtures (50% and 66% glycerol by weight) are shown in Fig. S1. Addition of polymers in the solvent increases

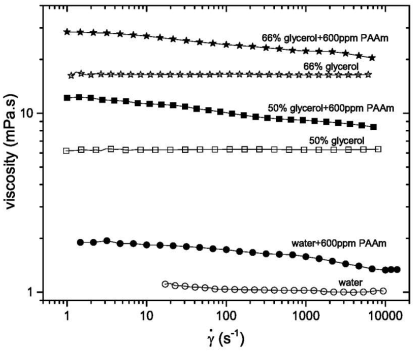

Figure 3.5: Shear-rate dependent viscosity of polymer solution (600 ppm PAAm; 5MDa, filled symbols) prepared in Newtonian solvent (open symbols): water and water-glycerol mixtures (50% and 66% glycerol).

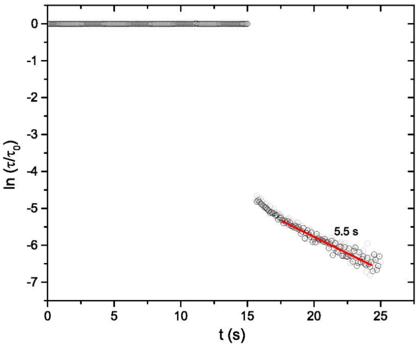

Figure 3.6: Measured shear stress upon cessation of steady shear flow at shear rates 5 s^{-1} (gray) and 10 s1 (black) for a polymer solution of 600 ppm (PAAm; 5 MDa) in 80% glycerol (viscosity=60.1 mPa.s). The red line is a linear fit to the data $\ln\frac{\tau}{\tau_0}$ versus time t, which yields $\lambda \sim 5.5$ s.

the solution viscosity nearly twice that of the solvent at low shear-rates and exhibits weak shear thinning behavior above intermediate shear-rates (Fig. 3.5). The viscosity ratio β of solvent and solution is estimated in the limit of zero shear rate at which the solution viscosity is independent of shear-rate.

To measure the longest relaxation time, polymer solutions (600ppm PAAm in 80% glycerol and 20% water) were subjected to a steady shear flow with shear rate ranging from 0.5 to 10 s^-1 for 15 s, and then the shear flow is steeply ceased [LJS09]. During this process shear stress is being monitored. Figure S2 shows typical relaxation of the stress upon cessation of shear flow at shear rates of 5 s^-11 and 10 s^-1. The measured stress decays exponentially as

$\frac{\tau}{\tau_0}\ e^{\frac{-t}{\lambda}}$ which yields the longest stress relaxation time λ 5.5 s. Here, τ_0 is the shear stress value at the shear-rate imposed. As in the dilute concentration range λ varies linearly with the solvent viscosity [LJS09]], we extrapolate the values measured at high solvent viscosities to lower solvent viscosities up to water. However, when compared to the relaxation times obtained by Capillary Breakup Extensional Rheometer (CaBER) (e.g. [SDH$^+$13]), which imposes a pure elongational flow as opposed to a shear flow, the relaxation times obtained in the present study (for 5 MDa PAAm) are substantially longer. It has been shown already in earlier studies that the relaxation times obtained from the stress-relaxation method are much higher than those obtained from CaBER measurements[ZGRW10].

CHAPTER 4

Turbulence in viscoelastic fluids at low and high inertia

Section 4.2 of this chapter is based on the manuscript titled "Turbulence in viscoelastic fluids at low and high inertia", authored by Sarath Sankar Suresh and Björn Hof. As the manuscript is not yet submitted for publication, the authors retain the copyright. The content is reproduced here for non commercial academic purposes, with proper attribution to the original authors. The version included here reflects the submission at the time of writing; please note that it is subject to change during peer review and before any eventual publication. All experiments are an original work by the author of the present thesis

4.1 Abstract

Polymeric liquids are abundant in nature, and the associated viscoelastic material properties fundamentally impact the flow dynamics, causing instabilities and turbulent-like motions at low and even at vanishing inertia. Conversely at high inertia polymer additives stabilize flows and reduce turbulent friction losses in pipe and channel flows up to an asymptotic limit. We here show that these seemingly opposing effects of viscoelasticity at low and high Reynolds numbers are rooted in the same phenomenon, the state of 'elasto-inertial turbulence' (EIT). By resolving the three-dimensional velocity fields in experiments we demonstrate that flows in these two regimes have the identical structural composition, lacking any features of inertial turbulence. Overall our findings suggest that just as Newtonian turbulence is the default state of ordinary fluids at high inertia, elasto-inertial turbulence governs viscoelastic fluids at sufficient shear, irrespective of inertia.

4.2 Results

For shear flows high inertia is synonymous with turbulence. Once the ratio of inertial to viscous forces, i.e. the Reynolds number (Re), is sufficiently large (e.g. $Re > 2000$ in pipes) inertial turbulence (IT) prevails. This standard picture only takes viscous material properties into account, but many fluids relevant in nature and applications are more complex and in addition to being viscous they are also elastic. This applies to solutions of (bio)polymers just as it does to blood, paint and polymer melts. The elastic fluid properties can give rise to new types of instabilities and turbulent like motions at surprisingly low inertia[GS00, GS01][SDH$^+$13]. In spite of these destabilizing effects at low inertia, viscoelasticity at the same time suppresses turbulence (IT) at high inertia. Most strikingly the dissolution of small amounts of long chain polymers can reduce the drag of pipeline flows by as much as 80% [WM08, PLB08]. With increasing polymer concentration turbulence becomes more and more subdued, however the drag eventually saturates at a level intermediate between turbulent and laminar flow. This so called maximum drag reduction (MDR) limit is independent of the type of polymer and solvent used and once reached, flows remain weakly fluctuating, which traditionally has been interpreted as a residual of the original IT[VMS70, SW00]. Along similar lines other studies suggested that the maximum drag reduction asymptote corresponds to the edge state of inertial turbulence and has a purely Newtonian originXiGra10,XiGra12.

A standard example in this context is the phenomenon of polymer drag reduction [WM08, PLB08], where inertial turbulence (subdued to a marginal state) is believed to persist even for high polymer concentrations. Starting from a turbulent flow of a Newtonian solvent, the addition of minute amounts of long chain polymers has been found to lead to a substantial drag decrease, an effect commonly exploited in oil pipelines. While initially the drag drops in proportion to the polymer concentration, it eventually saturates at a level intermediate between turbulent and laminar flow. Also known as the maximum drag reduction (MDR) asymptote, this limit surprisingly is independent of the type of polymer and solvent used. This MDR state is believed to originate from, and to be dynamically connected to inertial turbulence[VMS70, SW00, XG10, XG12].

More recently and by focusing on the transition to chaotic motion in such dilute polymer solutions, Samanta et al.[SDH$^+$13] have been able to distinguish a low inertia dynamical state, dubbed elasto-inertial turbulence (EIT), from Newtonian turbulence and proposed a fundametnally different interpretation of the MDR asymptote. Specifically these authors suggested that the elasto-inertial instability keeps flows from relaminarizing and that EIT may ultimately be responsible for the friction to settle to a level intermediate between Newtonian turbulence and laminar flow.

A definite link between EIT and MDR has however remained difficult to establish, and evidence is limited to moderate Reynolds numbers just exceeding the transition threshold of Newtonian turbulence ($3000 < Re < 6000$) [CLH18a**?** , SMW$^+$19, CSD20, ZX21, KSS21]. Simulations rely on constitutive models to mimic the action of long chain polymers and it is at present unknown if the structures observed here capture those in actual flows of viscoelastic fluids. While such distinct flow structures associated with EIT are identified for such low-Re MDR flows, depending on computational parameters also characteristic IT structures are found. Experiments on the other hand can in principle cover large parameter ranges, but they have so far not been able to resolve the full flow structure of EIT to permit a comparison and verification of model predictions. Nor has it been possible to resolve the three dimensional structure of high inertia, high elasticity flows, i.e. flows in the MDR limit, to test if eventually inertial turbulence prevails.

By resolving the structure of turbulence in experiments of dilute polymer solutions we demonstrate that at sufficient elasticity flows are governed by a single dynamical state, irrespective of inertia. Specifically we show that in the high inertia maximum drag reduction limit inertial turbulence structures are absent and that flows are instead dominated by sheet like structures and spanwise near wall vortices characteristic for EIT.

Experiments have been conducted in a D=20mm pipe with a length of L=5500mm and hence an aspect ratio of L/D=275. The flow was driven by two pistons (each has a diameter 125 mm and a stroke length of 1200 mm) that were traversed by a linear stage and simultaneously push the fluid through the pipe at a constant rate. As a Newtonian solvent we used water and added polyacrylamide (PAAm) with a molecular weight of 18 million Da. Polymer concentrations were increased in discrete steps while monitoring the drag using a commercial pressure sensor(Validyne DP15). The flow structure was measured simultaneously using PIV. For PIV the fluid was seeded with a small fraction of tracer particles (hollow glass spheres with a diameter of 13 microns), and illuminated by a laser light sheet (approximately 0.5 mm thick) in an $r-\theta$ (radial-azimuthal) plane located 150 D from the pipe inlet. Two high speed 4Mpixel cameras were used to record particle images at frequencies of up to 4500 Hz. A commercial software package (DAVIS 8, Lavision) has been used to reconstruct the velocity fields and further processing was carried out using Matlab.

We initially visualize vortex patterns in the measurement plane. Respectively the streamwise vortictiy (ω_z) is shown for Newtonian turbulence at $Re = 8000$

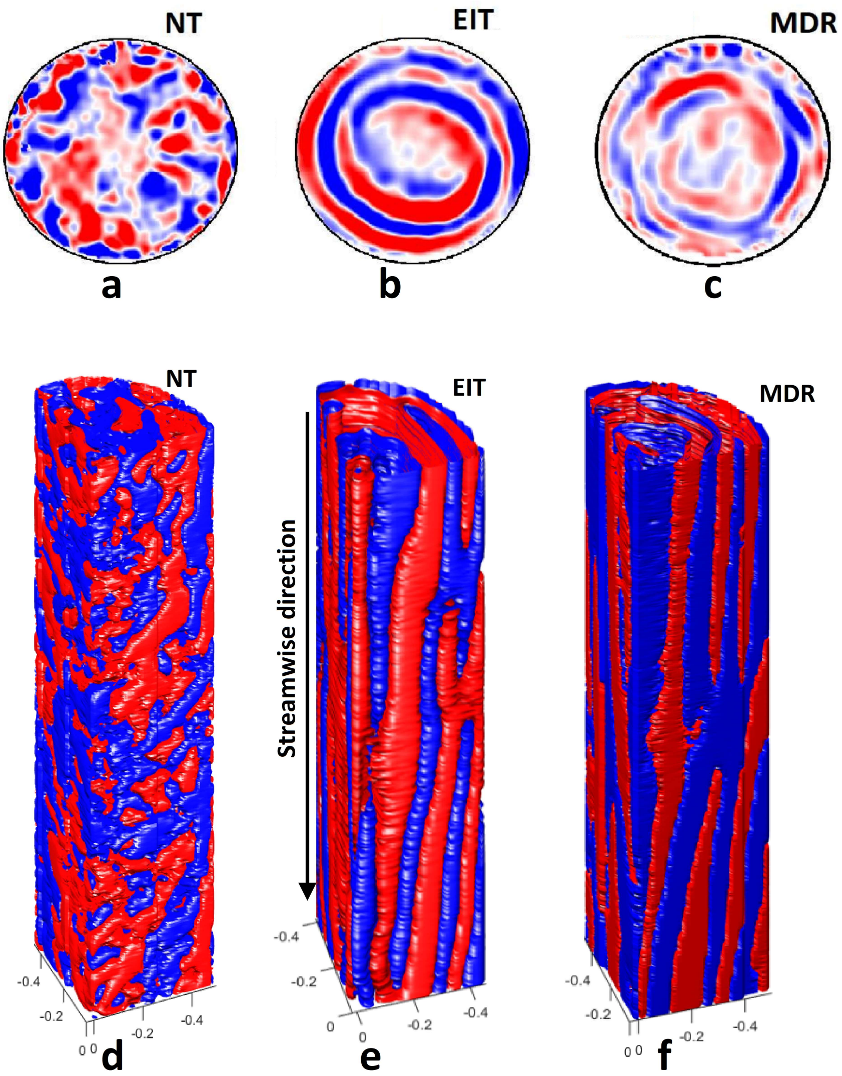

Figure 4.1: Structure of turbulence in Newtonian and viscoelastic fluids. a-c Streamwise vorticity is shown in an azimuthal radial cross-section of the pipe for a Newtonian turbulence at Re=8000, b the flow of a viscoelastic fluid in the MDR limit (a 100ppm PAAm solution at Re = 11720, Wi = 47.8125 E = 0.004) and c EIT for a 200ppm PAAm (63 percent glycecrol) solution at Re = 1750, Wi =93.75 E = 0.0536. d,e show 3D reconstructions of the streamwise vortex structure of MDR d and EIT e flows. To highlight the azimuthal-streamwise vorticity sheets characteristic for EIT and MDR, only a slice of the full flow field is shown. Note that the streamwise direction is reconstructed from the time sequence of the measurements in the azimuthal radial(same as a-c) cross-section by applying Taylor's frozen turbulence hypothesis (i.e. assuming that the streamwise advection is fast compared to structural changes).

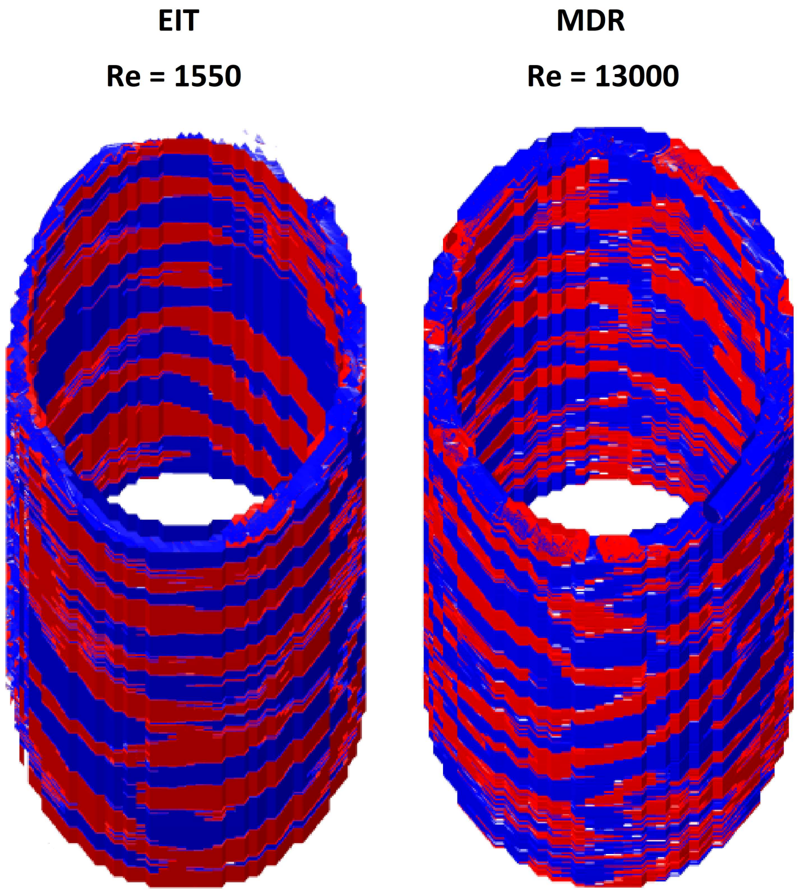

Figure 4.2: Near wall structure of EIT and MDR. Isosurfaces visualize the second invariant of the velocity gradient tensor, Q. Positive values (red) indicate rotational flow while negative (blue) values indicate extensional motion. Viscoelastic flows at low and high inertia are dominated by azimuthally extended alternating regions of rotational and extensional flow. Such structures had been predicted in numerical simulations of elasto-inertial turbulence, but so far could not be confirmed in experiments. As shown the high Reynolds number flow in the maximum drag reduction limit features the same Q-structural composition as EIT.

in Fig.1 a. Red (/blue) isosurfaces correspond to positive (/negative) values of ω_z and in this case the turbulent vorticty field is composed of irregular patches and shows no clear pattern. This qualitatively changes when sufficient amounts polymers are added and the flow enters the MDR limit. For a 100ppm concentration of PAAm at identical Re, vorticity arranges in azimuthal, ringlike structures, concentric to the pipe wall (panel b). This composition of layers in the radial direction is reminiscent of near wall sheets that have been reported in simulations[SDH$^+$13, DTS13] of viscoleastic flows at lower Reynolds numbers, specifically in the limit of EIT (albeit for a different quantity, polymer stretch, which is not accessible in experiments). To compare these flow structures to low Reynolds number EIT flows we next conducted experiments with the same fluid in an aqueous 200ppm solution mixed in 63% glycerol solution at $Re = 1750$. As shown in panel c, EIT is equally composed of azimuthal vorticity rings, in qualitative agreement with the MDR flow at much higher Reynolds number.

Although measurements are carried out in an r-θ plane and hence a single measurement does not provide any information on the streamwise flow structure, images are sampled at high frequency while turbulence is advected through the measurement plane. Assuming that the turbulent internal dynamics are much slower than the bulk advection (Taylor's frozen turbulence hypothesis), the temporal information can be used to approximate the spatial structure. This allows the reconstruction of the 3D flow structure shown in panels d, e. Rather than showing the data for the entire pipe we visualize streamwise vorticity for an azimuthal slice and here it becomes apparent that the characteristic structures of MDR (d) as well as of EIT (e) are azimuthal vorticity sheets that in a cone like fashion stretch from the wall towards the pipe centre.

It is noteworthy that these vorticity sheets are not limited to the near wall region but penetrate towards the pipe centre (covering what in ordinary turbulence would be considered the logarithmic layer and part of the wake). Whereas simulations of MDR flows[ZX21] reported Newtonian turbulent structures (hairpin vortices) to persist in MDR flows, such features cannot be found in experiments. Numerical simulations on the one hand can only be carried out at considerably lower values of Re and albeit the Weissenberg number (Wi, ratio of elastic to viscous forces) is nominally very high, such model simulations are known to require far larger Wi values than experiments to capture the corresponding phenomena. It is hence unclear if simulations have truly reached the elasticity dominated limit yet.

In order to compare the characteristic structures of EIT to numerical predictions we compute Q, the second invariant of the velocity gradient tensor. As shown in Fig. 2a, and again making use of the Taylor hypothesis. This quantity is dominated by near wall structures that are elongated in the azimuthal direction. Specifically positive Q isolevels (red) indicate rotational flow while negative values (blue) indicate regions of extensional flow. The azimuthal Q structures observed are in excellent qualitative agreement with model simulations[SDH+13, DTS13**?**] of EIT where Q isosurfaces equally are extended in the azimuthal direction (/spanwise in channel flow). Plotting the same quantity in a 100ppm PAAm aqueous solution at Re=13,000 in the maximum drag reduction limit, Fig. 2b, reveals qualitatively the same spanwise extended near wall structures and consequently shows that the characteristic EIT features persist and continue to dominate the flow at high inertia.

It is noteworthy that the the observed structures reported in Figures 1 and 2 correspond to a wall mode, i.e. the fluctuation amplitudes reach their maximum some distance from the wall and drop towards the pipe centre. This feature is typical for EIT considerably far from onset as reported in recent experiments. Conversely, close to onset the flow structure corresponded to a centre mode in agreement with the travelling wave predicted by linear stability analysis[GCK+18]. Moreover numerical studies identified a subcritical route via a nonlinear travelling wave, which are equally dynamically connected to the centre mode instability. The origin of the wall mode and the associated Q structures that dominate EIT away from onset and persist across a vast parameter range, remains an open question.

Finally we compare the velocity spectra of EIT to those at high Reynolds numbers in the MDR limit. Due to the high sampling frequencies required, the velocity time series were measured using Laser Doppler Velocimetry (TSI PowerSight Laser module), from which Energy spectra are calculated using arrival-time quantisation [NDN18](see SI for experimental details). In the EIT regime, see Fig. 3 for examples at Re=5 and at Re=1,400 the spectral density falls off with an exponent close to -3. At high Reynolds number the same slope is found in the MDR limit (Re=21,000, E=0.0019, Wi=40.6), whereas for Newtonian turbulence a significantly shallower slope (close to the expected -5/3) is found. Note that in this Re range for Newtonian turbulence the inertial range is not sufficiently developed to show an appreciable scaling range. The difference between the viscoelastic and Newtonian runs at high inertia is nevertheless evident and again the agreement between EIT and MDR flows is excellent.

Interestingly -3 exponents were recently reported for elasto inertial turbulence in a jet flow [YKR+21] and also in an earlier study of grid driven turbulence[VM13]. For the latter case the authors however explicitly assumed that their observations

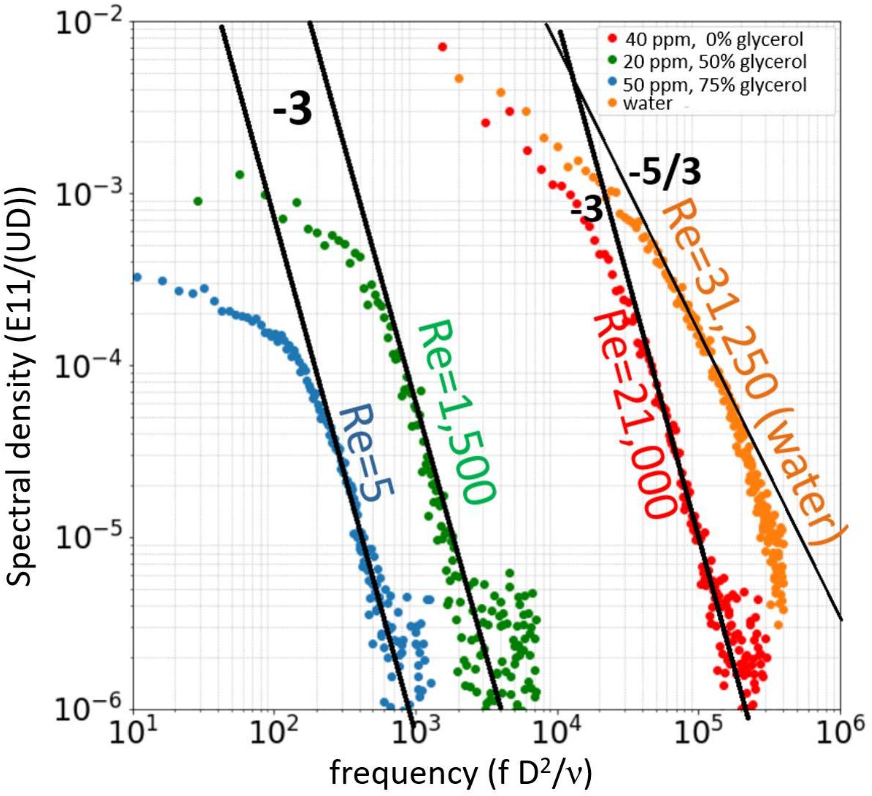

Figure 4.3: Energy spectra. Spectra are computed from velocity time series measured half way between the pipe wall and the pipe centre using LDV. The Re=5 data were measured in a smaller diameter (D=4mm) pipe [CLV+21] and in this case a 50ppm PAAM solution was used, where the solvent was a 75% glycerol 25% water mixture. All other measurements were carried out in the standard 20mm pipe. At Re=1,500 (E=0.11, Wi=175) a 50% glycerol water mixture was used with a concentration of 20ppm PAAM. In both these cases the flow showed the weak fluctuation levels characteristic for EIT. In this limit spectra show a -3 slope. The same slope is found in the MDR limit at much higher Reynolds number (Re=21,000, E=0.0098, Wi=206, 40ppm of PAAM in water). For comparison we show a Newtonian spectrum at similar Re= 31,250. Note that for Newtonian pipe flow at these Re the inertial range (-5/3 scaling) is only about to develop.

are unrelated to EIT (or as they called it “structural turbulence"[OA26]) because of the high inertia levels. This traditional Newtonian turbulence perspective misses the key point that the elasto-inertial instability is not governed by the Reynolds number but instead by the shear rate [Rei26, SDH$^+$13] or in dimensionless terms the Weissenberg number. Viscoelastic fluids may hence exhibit Newtonian turbulence provided that the Reynolds number is sufficiently large while the Weissenberg number is moderate, as is the case in the drag reduction regime of dilute polymer solutions. The established paths towards the MDR asymptote involve either an increase in velocity, and hence shear, or an increase in polymer concentration. Crucially both these routes correspond to an increase in the Weissenberg number and hence will eventually give rise to elasto-inertial turbulence. We argue that it is precisely this unavoidable instability that keeps high shear viscoelastic flows from relaminarizing and gives rise to a characteristic friction scaling. On the low inertia side, we tracked EIT to Reynolds numbers of order unity, it is presently unclear if the state persists to the zero inertia limit [KSS21, LLM24], or if, as the name implies, a non-vanishing inertial contribution is required. Interestingly the spectral exponents measured in our study are actually close to the prediction for the latter inertialess limit and the corresponding state of purely elastic turbulence [GS00]). In this case exponents smaller than -3 are expected [FL03]).

Our study demonstrates that viscoelastic fluids exhibit a unique state of turbulent motion provided that the shear rate is sufficiently large. This state of elastoinertial turbulence is hence not limited to low Reynolds numbers, but equally entails the high inertia phenomenon of maximum drag reduction. The structural composition identified here bridges the gap to computational studies of EIT and moreover, the spectral signature identified suggests a link to jet flows and to isotropic turbulence of viscoelastic fluids. Based on these findings we propose that EIT is as central to the motion of viscoelastic fluids as ordinary turbulence is to Newtonian fluids.

4.3 Transition from Newtonian turbulence to MDR

In the previous section we have looked at the characteristics of EIT and MDR, and sought to display the connection between the EIT and MDR state, showing incredible similarities between the topological structures in the two states, suggesting that MDR is equivalent to EIT at high Re. The question arises where, en route from NT to MDR friction scaling, do these structures arise, and whats the nature of the development of these structures as we consistently

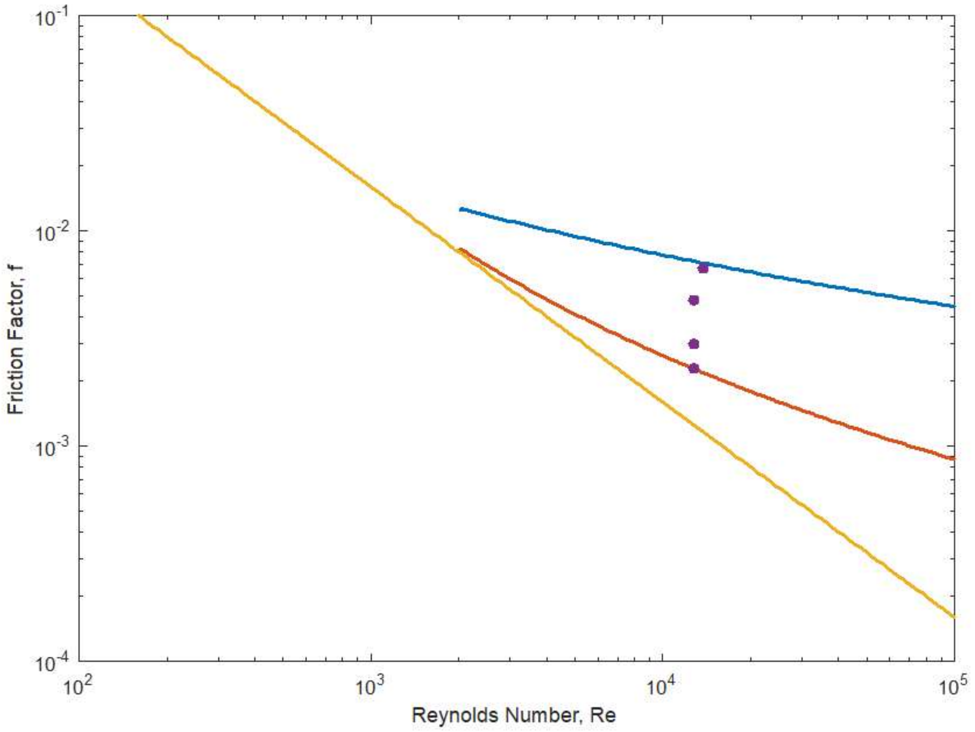

Figure 4.4: Friction factors at constant Re, as one goes from NT to MDR. From top to bottom, the points correspond to 2, 8, 10, and 12 ppm, Re maintained at 14000

increase E in a constant Re and β. For these low concentrations on en route to MDR, we find that the viscosities vary in amounts within measurement errors of the rheometer, hence the assumption of constant β is justified. Fig. 4.5 and fig. 4.7 demonstrate this transition as we go from purely turbulent flow to maximum drag reduction, via streamwise velocity and streamwise vorticity plots.

Fig. 4.4 shows the friction factors corresponding to the four transitional points as the flow transitions from NT to MDR. The 2 ppm and 8ppm runs are closer to NT, although the 10ppm is in the so called HDR-regime, based on friction factors. The 12ppm run is on MDR, and we also do a further small increase in the concentration at this point to 13ppm, to make sure we capture the dynamics into the MDR regime a bit. Looking at the velocity fluctuations in Fig. 4.5, the first three panels seem to have different characteristics than the ones closer to MDR. Below 8ppm, one sees more chaotic and stronger fluctuations that are NT-like, lacking the characteristic long streaks associated with EIT, The effects of drag reduction are clear right from the get-go, as

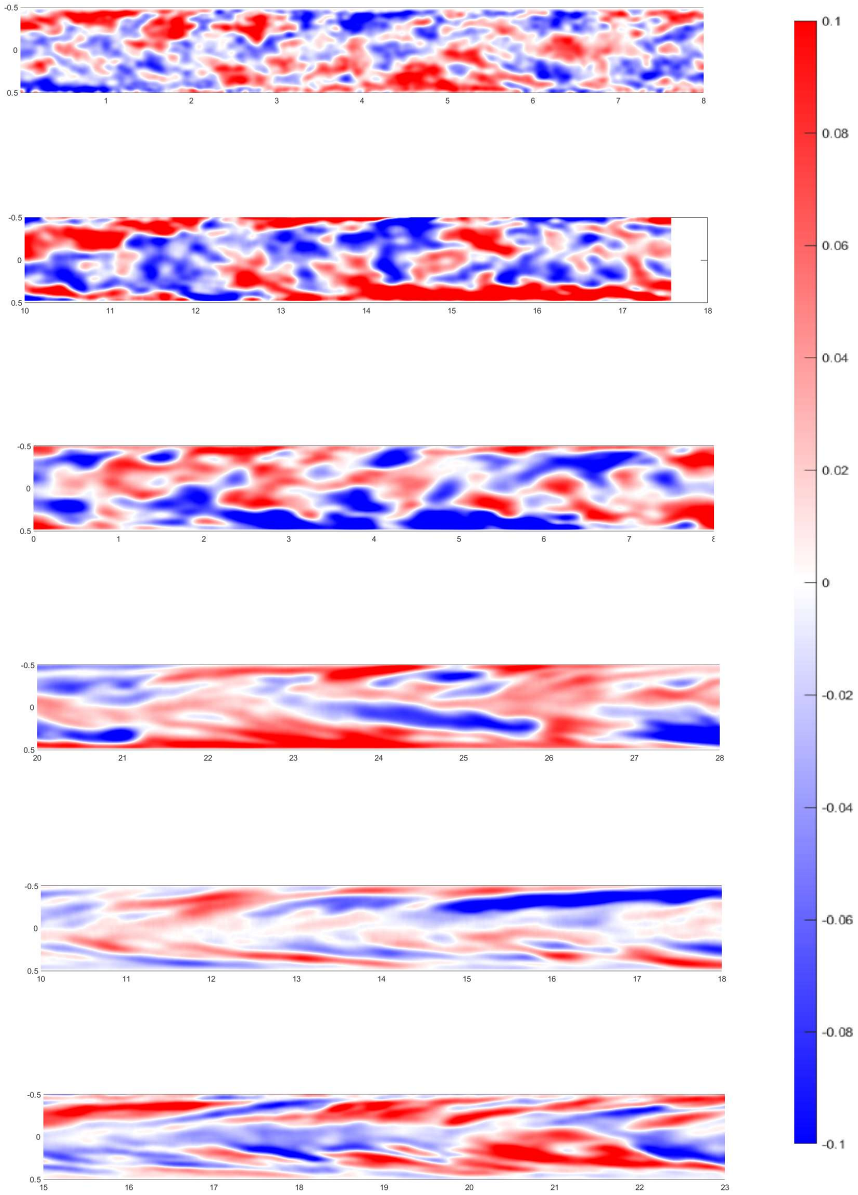

Figure 4.5: Streamwise velocity fluctuations in a 20mm pipe, flow is from right to left. The panels correspond, from top to bottom, 2ppm, 8ppm, 10ppm, 12ppm, 13ppm, at Re maintained roughly at 13000

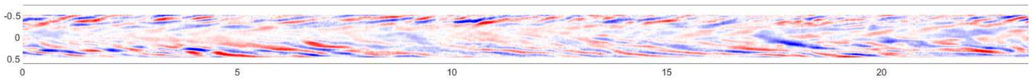

Figure 4.6: Long experimental run of flow at 13ppm, with very ordered and alternating streaks of vorticity adjacent to the wall, Re = 13000

the 2ppm runs already shows chaotic, but characteristically larger structures in the streamwise vorticity fields. The surprising thing though is that the vorticity structures that arise until we reach MDR are slightly different from the last panel we show. The long elongated structures of vorticity (also velocity), although they start appearing around the 10 ppm mark, do not take a neat ordered shape until we are well within MDR, at 13ppm. It can be seen from the runs at 10 and 12ppm, how the structures of vorticity are markedly less inclined, and and tend to get lifted into the bulk flow, evident from the way these structures bend towards the pipe centre in panel (d) and (e) in Fig.4.7.

Although the structures associated with EIT start appearing starting from high drag reduction regimes, as has been noticed by studies before, the dynamics change starkly while one reaches MDR, and the structures appear more coherent and regular, see fig. 4.6. The figure shows the presence of regular inclined vorticity streaks, all across the pipe length measured, there is no intermittent phenomenon seen in this case between NT and EIT. It is also notable that the presence of structures near the centre of the pipe has also seen a decrease.

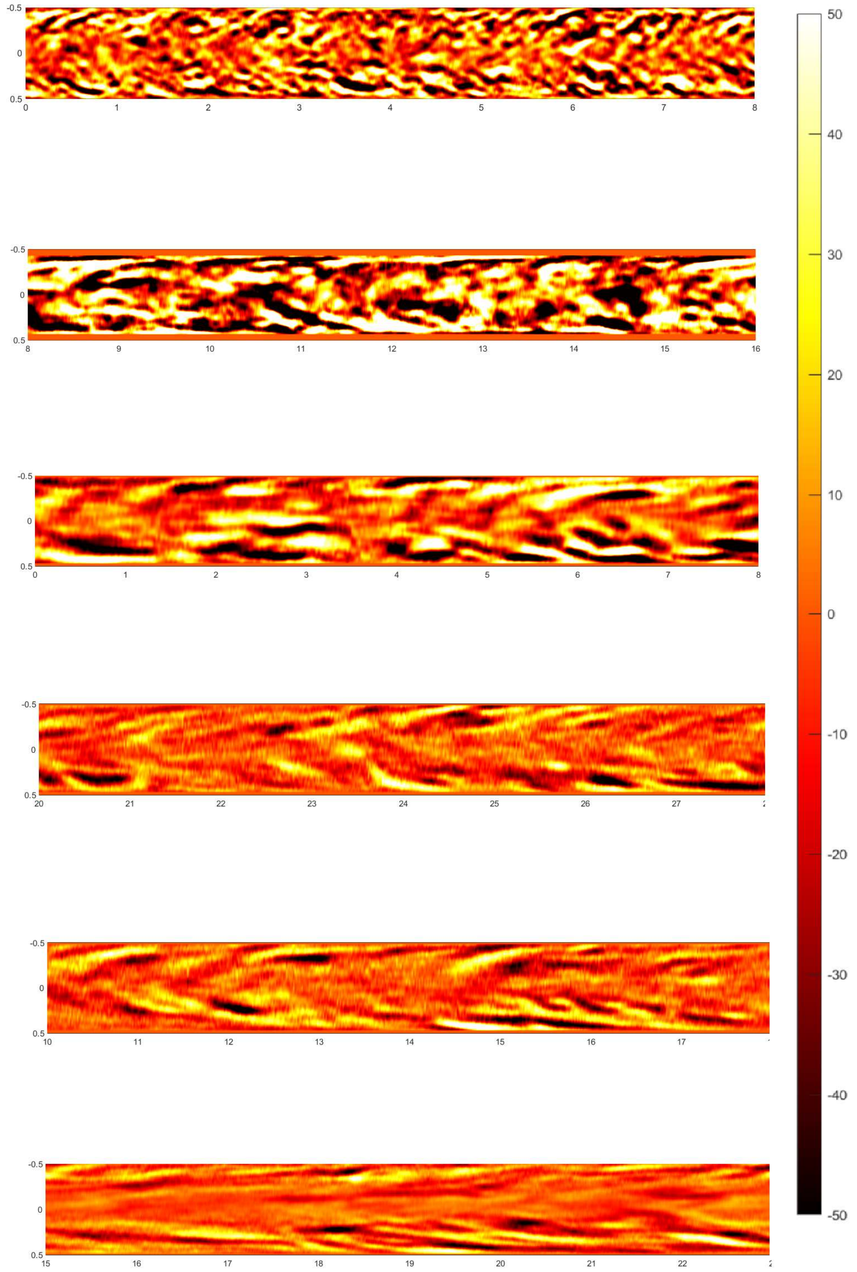

Figure 4.7: Streamwise vorticity in a 20mm pipe, flow is from right to left. The panels correspond, from top to bottom, 2ppm, 8ppm, 10ppm, 12ppm, 13ppm

This further elucidates the point made in the previous section about MDR specific dynamics resembling closely with the wall mode that we've seen before. Along with the topological structures based on the Q-value, we demonstrate that the flow at high drag reductions are EIT dominated, but at MDR, the dynamics are exactly like at wall modes that we observe at $Re < 2000$.

4.3.1 Structures at higher concentrations

Historically, the MDR asymptote has been proven to be asymptotic only in the dilute regime of polymer concentrations, and in his original work, Virk limits the claims of the drag reduction asymptote to polymers which fall into this dilute category. This brings out the question about what happens when the concentration of the polymers is further increased. For such high molecular weight polymers, these regimes haven't been studied much in the context of EIT. Experiments are performed for a 500ppm solution for $Re = 4000$ and $Re = 5300$.

Looking at the streamwise velocity fluctuations as before, we find surprisingly that for Re as high as 4000, we see long regions of almost constant streamwise velocities, for lengths as long as 20 diameters. These long streaks occupy the whole pipe diameter, and show little internal dynamics. The same can be said about the streamwise vorticity, with the regions corresponding to the inactive regions to display almost full vortex suppression. Conversely, in the regions where we do find fluctuations, the vorticity structures are remarkably strong, and show the same alternating sheets of vorticity associated with EIT. Yet more surprisingly, for the higher Re, the streamwise fluctuations show much more activity and no longer contain the passive regions as at $Re = 4000$, but the same cannot be said about the vorticity. In fact the activity corresponding to the vortices are confined to much shorter regions.

This result could not be readily explained, and further experiments need to be done to understand this phenomenon. Considering the surprising results in this less studied regime, I propose that this could be a promising avenue for future research.

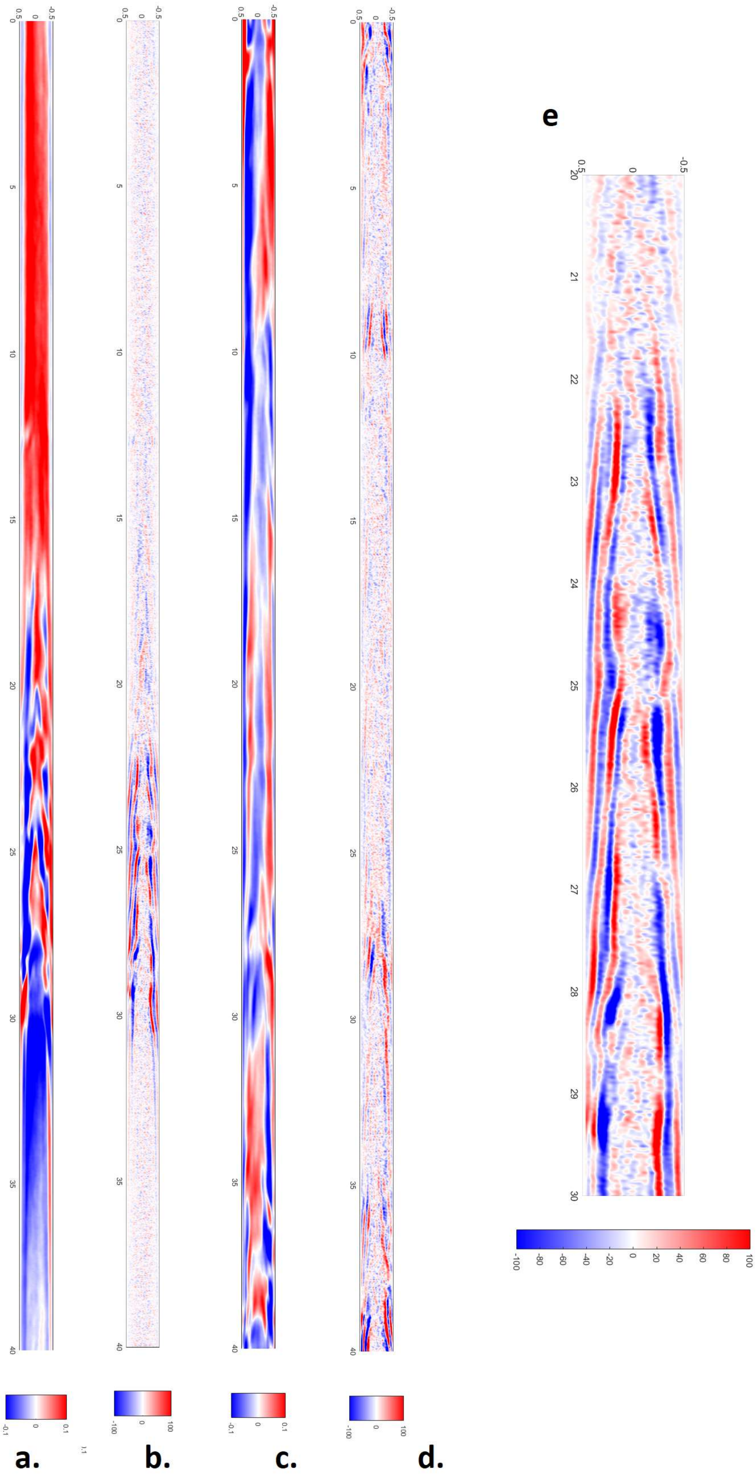

Figure 4.8: Flow structures at 500ppm, (a),(b): velocity and vorticity structures at $Re = 4000$, and (c),(d): $Re = 5300$ (e): zoomed in vortical structures of the active region at $Re = 4000$

CHAPTER 5

Low Inertia limit of Elasto-inertial turbulence

This chapter reproduces the manuscript titled “Low Inertia limit of Elasto-inertial turbulence” authored by Shoaib Kamil, Jose Lopez, Sarath Sankar Suresh and Björn Hof, currently under review. Since the manuscript has not yet been accepted, copyright remains with the authors. The version included here reflects the submission at the time of writing and may be revised during peer review.

Author contributions: The present author has visualised the velocity fields from stereo-PIV calculations, and made subsequent numerical analysis.

5.1 Abstract

Pipe and channel flows of viscoelastic fluids display chaotic dynamics at unusually low speeds, a phenomenon referred to as elasto-inertial turbulence, EIT. Despite much recent progress, the state's origin and a possible connection to purely elastic turbulence, ET, a dynamical state encountered in curved streamline flows, remain debated. We demonstrate that in pipe flow experiments EIT has a minimum inertia and maximum elasticity number limit, and that hence the instability is not of purely elastic origin. Moreover we identify distinctive coherent structures that dominate the dynamics of EIT, and that are in remarkable agreement with a nonlinear travelling wave, the "arrowhead", previously discovered in two dimensional model simulations. This finding pinpoints the nature of the EIT onset and at the same time suggests that the turbulent dynamics appears to evolve around a limited number of unstable states, opening avenues for low-dimensional modelling approaches for future studies.

5.2 Results

The addition of minute quantities of long chain polymers to a Newtonian solvent can fundamentally alter the motion of fluids. At high Reynolds numbers (Re), polymers dramatically decrease the drag of turbulent flows[WM08], a property frequently exploited to reduce pumping costs in oil pipelines. In contrast to this stabilizing effect, polymers cause instabilities[LSM90, Sha96, MPÖ96] and novel states of turbulence[GS00, GS01, SDH+13, YKR+21] at low Reynolds numbers, a regime in which Newtonian flows are perfectly stable and laminar. Even though such low Reynolds number turbulent motions have already been reported for pipe flow close to a century ago[OA26, Rei26], their origin remains heavily debated[DTH23]. Various studies proposed a link to a hoop stress instability that occurs in flows with curved streamlines[LSM90] and here leads to purely elastic turbulence[GS00, GS01]. While this instability cannot arise linearly in straight pipes and channels, it has been suggested to arise nonlinearly, i.e. following from perturbations of finite amplitude[BMW+03, MvS05, PMWA13, MvS19].

More recently, a different linear instability mechanism[GCK+18, KCG+21] has been discovered for viscoelastic pipe and channel flows, i.e. a mechanism that does not require curved streamlines and is not driven by hoop stresses. Instead it corresponds to a centre mode instability and involves a balance between inertia, viscous and elastic stresses[GCK+18]. For increasing elasticity of the constitutive model (Oldroyd-B) the critical Reynolds number of this instability was found to decrease with a power law. However, for sufficiently large elasticity the instability ceases to exist, setting a minimum Reynolds number (≈ 80 in Oldroyd-B fluids) for the onset. An exception is the ultra dilute highly elastic limit (parameters very far from actual polymer solutions) in which the instability can persist to zero inertia [**?**]. It is noteworthy that an upper elasticity number bound is specific to the centre mode instability and conversely does not arise for the competing scenario of the aforementioned purely elastic hoop stress instability[LSM90]. On the one hand the persistence of EIT in pipe experiments to elasticity numbers[CLV+21] that are an order of magnitude larger than those of the linear centre mode instability may be regarded as support of such a purely elastic scenario. On the other hand the flow structures that were observed in these same experiments at onset have been found to resemble the centre mode[CLV+21]. Channel experiments[PMWA13] reported chaotic flow even at vanishing inertia ($Re < 10^{-2}$) and elasticity numbers $O(10^3)$, a finding that supports a subrcritical purely elastic transition route.

An alternative explanation for the high elasticity numbers and low Re observed is that the centre mode instability at this point occurs subcritically, in line with sim-

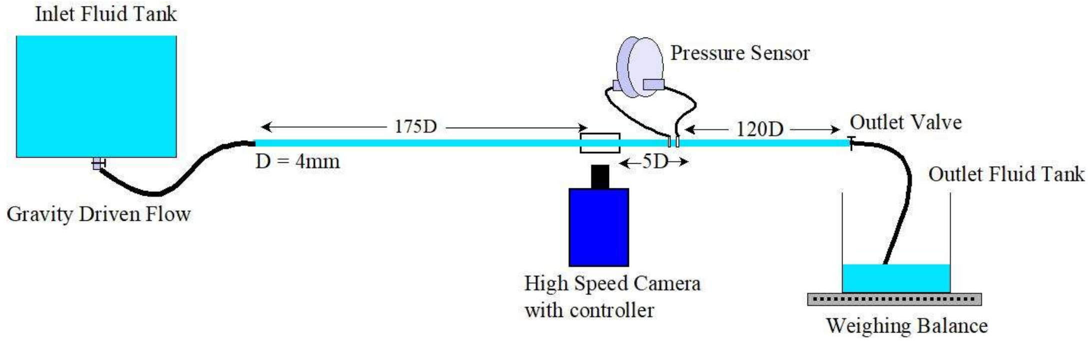

Figure 5.1: Schematic of the experimental set up. The flow through the 300D long pipe is gravity driven. Measurements of pressure fluctuations and the velocity fields (by planar particle image velocimetry) were carried out 175D from the entrance where the flow was found to be independent of the inlet conditions. The flow rate was determined by measuring the weight of the fluid collected in the outlet tank.

ulations of two dimensional channel flow [PDK20, DPK+22, WSZ21, BPK22]. This subcritical branch arises from a nonlinear travelling wave, referred to as the "arrowhead". Subsequently the arrowhead could be continued to negligible inertia[Mor22] where it supports a purely elastic form of turbulence[LLM24].

Finally, other studies[SMW+19, SMMG21] put forward a very different transition scenario, suggesting that EIT does not arise from elastic modes but essentially from a Newtonian solution branch, i.e. Tollmien-Schlichting waves. Computations in minimal channel flow units[ZCW+24] recently argued in favour of this latter scenario based on observations of wall modes for sufficiently large domain sizes whereas arrowhead structures (favouring a subcritical centre mode route) were only found for the smallest domain sizes. While wall modes are also found to dominate the dynamics of actual EIT in experiments[CLV+21], in this case the high amplitude near wall structures were found to only arise significantly above onset, whereas closer to onset flows were dominated by the aforementioned centre mode structures.

As we will show in the following, in pipe flow experiments the onset of EIT follows a simple scaling with elasticity number. This scaling persists to elasticity numbers as large as 200 but upon a further increase the transition threshold is found to diverge and the instability ceases to exist. This low Re, high E limit in experiments rules out that EIT originates from a purely elastic (i.e. subcritical hoop stress driven) instability [BMW+03, MvS05, PMWA13, MvS19]. Instead, the scaling and the divergence of Re_c qualitatively agree with the general shape of the neutral stability curve of the centre mode instability[GCK+18]. The order of magnitude lower Re, and two orders of magnitude higher E values however support the corresponding subcritical route. We eventually resolve the transition route by monitoring the flow fields. Throughout the parameter space explored the dominant flow structure of EIT close to onset, consists of symmetrical bullet shaped streak formations that are in surprisingly close agreement with the arrowhead, and hence with the nonlinear travelling wave expected for the subcritical centre mode instability.

Experiments were carried out in a $D = 4mm \pm 0.01$ diameter precision bore glass pipe, 300 D in length. To determine the deviation from laminar in polymer solutions we monitored pressure fluctuations using a differential pressure sensor (Validyne DP45) as illustrated in Fig 5.1. Moreover, we recorded velocity fields in the mid-plane (streamwise-radial) of the pipe using a high speed particle image velocimetry, PIV, system (LaVision GmbH). The flowrate was monitored using a precision balance (321 LX) and the temperature was recorded using a PT 100 probe (not shown). The working fluid was a 50ppm solution of polyacrylamide PAM (18 million Da) in water-glycerol mixtures of varying viscosity. The fluid's relaxation time was determined using an Anton Paar rheometer (MCR 105). For the PIV measurements the fluid was additionally seeded with a small amount of 3 micron sized silicon carbide (SiC) particles.

Flows were found to be laminar at sufficiently low speeds (or low shear rates). In this steady flow regime, pressure fluctuations were indistinguishable from the sensor's intrinsic noise level. Upon increasing the Reynolds number, the pressure fluctuations would eventually exceed this baseline level at a critical threshold as shown in Fig 5.2. As in previous studies of the onset of EIT [SDH+13, CLV+21] no hysteresis could be detected. For the aqueous 50ppm solution (Fig 5.2 a), the onset occurs at $Re \approx 270$ and here the transition is from laminar directly to a fluctuating, weakly chaotic flow state in agreement with earlier experiments [SDH+13, CSD18, CLV+21].

In order to push the threshold to lower Reynolds numbers, we increased the

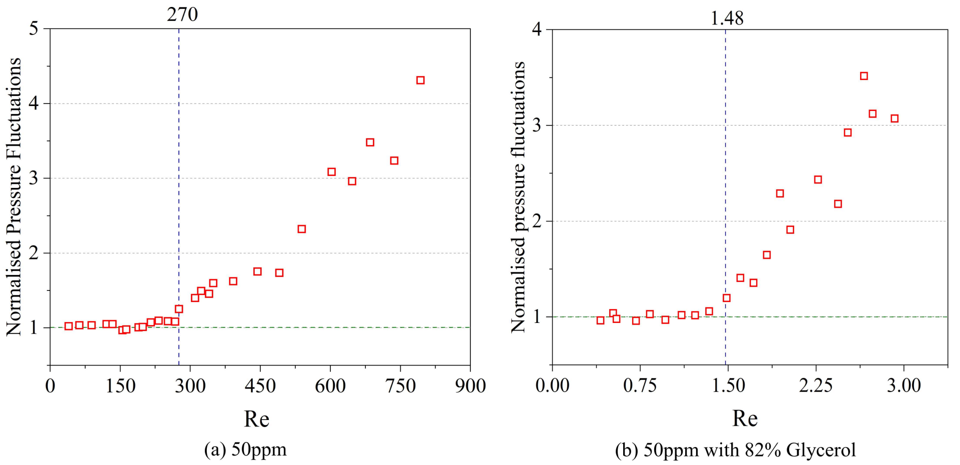

(a) 50ppm

(b) 50ppm with 82% Glycerol

Figure 5.2: Pressure fluctuations demarcate the onset of EIT. (a) pressure standard deviations for 50 ppm PAAm dissolved in water, and (b) for 50 ppm of PAAm dissolved in 82% glycerol and water mixture. The data is normalised by the respective sensor noise level in laminar flow. The bottom horizontal dashed lines indicates the laminar level. The vertical dashed lines approximately demarcate the onset of EIT.

fluid's elasticity number, $E = 8\lambda\nu/D^2$. Here λ is the polymer relaxation time and ν the fluid's kinematic viscosity. For simplicity and consistency, we chose to keep the polymer concentration constant (50ppm) and instead increase the viscosity by altering the glycerol concentration. This procedure allowed us to vary E between 0.04 and 450.

As a result, and as shown in Fig 5.3, the onset of transition (Re_c) drops by two orders of magnitude as E increases. While this emphasizes the importance of elasticity as the instabilities driving force [BPK22], eventually for $E > 250$ the instability disappears. At $E = 450$, the flow remained laminar even when the Reynolds number is increased above 100, whereas for slightly less elastic fluids, $E = 150$, the instability occurred at Re of O(1). The disappearance of the instability with increasing elasticity number is characteristic for the centre mode instability[GCK$^+$18] and as mentioned above would not be expected for a purely elastic, hoop stress driven instability[LSM90]. It is noteworthy that

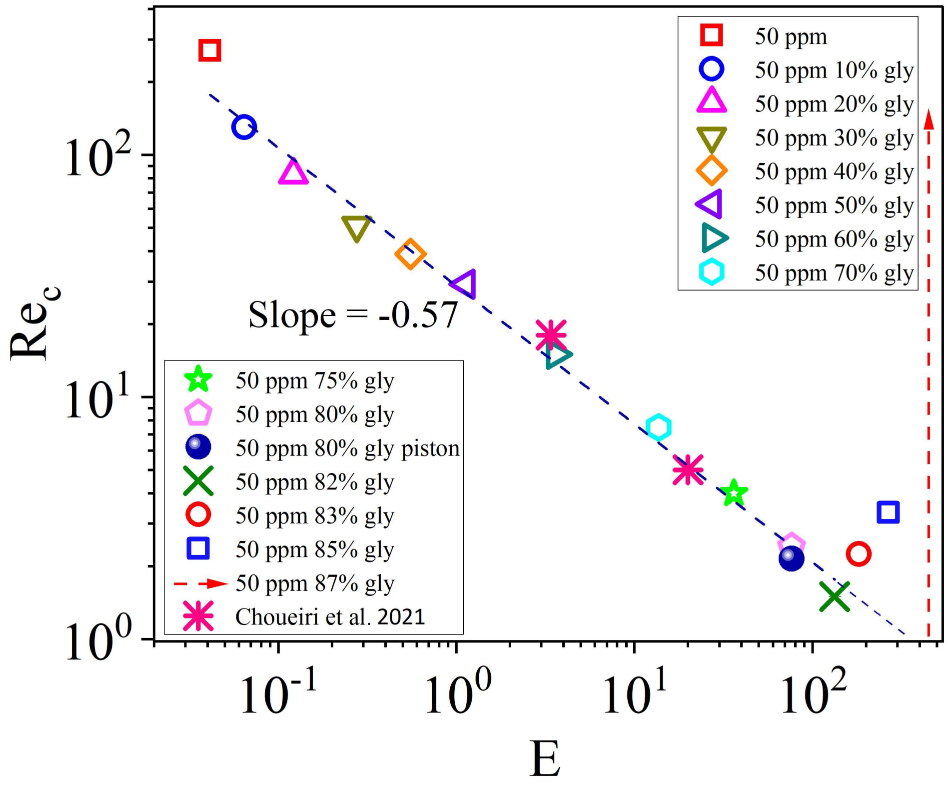

Figure 5.3: Comparison of critical Reynolds number (Re_c) as a function of elasticity number (E), including data from current experiments and [CLV$^+$21]. Re_c decreases with E following a power law with an exponent of -0.57 up to $E = 150$, after which is begins to to increase before the instability eventually disappears.The vertical dashed arrow line at $E = 450$ demarcates the onset of EIT at very high Reynolds number.

in experiments, even at the minimum Re_c, the transition is not to a steady state but the flow is immediately chaotic, which, as argued previously[CLV$^+$21] points towards a subcritical mechanism. Subcriticality also rationalizes that, in our case, the minimum transition threshold is of order unity, whereas for the linear stability analysis the minimum is close to 80 [GCK$^+$18]. This being said, quantitative comparison between experiments and theoretical predictions is not necessarily expected given that the latter rely on simplified constitutive models to mimic the polymer dynamics ([BPK22]).

Performing particle image velocimetry, we resolved the velocity field in the streamwise radial cross section as shown in Fig 5.4. Plotted are the deviations from the time averaged mean profile, visualizing low- (black) and high- (red) speed streaks. While the flow patterns are typically weakly chaotic (see panel (e)), the streaks frequently form close to symmetric bullet-shaped structures

(Fig 5.4 (b)-(e)) in the central part of the pipe. This coherent flow structures closely resembles the aforementioned arrowhead state Fig 5.4 (a), and are observed to dominate the onset of EIT for all the elasticity number investigated. As previously discussed the underlying arrowhead travelling wave bifurcates from the centre mode wave and in doing so manifests a sub-critical branch.

In the context of Newtonian turbulence, nonlinear (unstable) travelling waves, equilibria, and periodic orbits are commonly referred to as invariant solutions or exact coherent structures, ECS [Ker05, ESHW07, KUVV12, GF21]. Not only do ECS play a central role for the transition from laminar flow, but just as for other chaotic dynamical systems [ACE$^+$87], their stable and unstable manifolds form the scaffold of the turbulent dynamics. Understanding the dominant ECS could help provide insights into turbulence and potentially be used to create models for predicting [STGS17] or even controlling [BMWH20] the dynamics.

While these approaches have recently gained much attention in Newtonian turbulence, they were typically limited to symmetry constrained (periodic domains etc.) situations[YHB21, CPST$^+$22, PNBK24] or two dimensional flows. In unconstrained pipe flows, specifically in experiments, only very few sightings of travelling waves have been reported [HVDW$^+$04, HDLKW08, DLMAH12]. The rapid increase of the attractor dimension detected during the transition in channel flow [PYD$^+$23] highlights the challenges encountered for such approaches in Newtonian turbulence.

The circumstance that coherent structures resembling the arrowhead can be experimentally detected, and their persistence across many pipe diameters (Fig 5.4 (e)), suggests that close to onset elasto-inertial turbulence is dominated by a relatively small number of unstable solutions, and hence that the methodology developed for inertial turbulence should be ideally suited for the problem at hand.

It is noteworthy that the minimum Reynolds number in Fig 5.3 for the onset of EIT is fluid specific. Therefore, for some combination of polymer concentration and solvent viscosity, potentially a lower minimum threshold and even the vanishing inertia limit may be reachable. Analogous to channel flow, where the arrowhead travelling wave[Mor22] and the associated subcritical transition[LLM24] have indeed been shown to persist to zero inertia. Irrespective of a possible link to an inertialess turbulent state, the circumstance that, for the given parameters, the instability disappears with increasing elasticity number is characteristic for the centre mode instability[GCK$^+$18] and sets this scenario apart from the competing view of a subcritical, hoop-stress driven transition[BMW$^+$03, MvS05, PMWA13, MvS19].

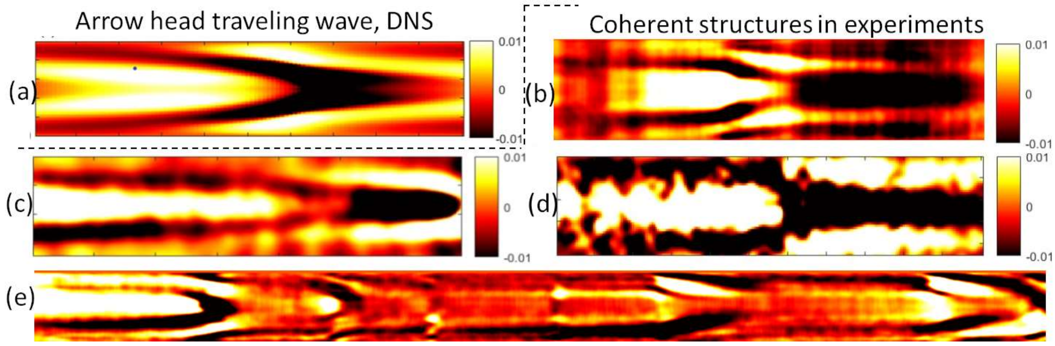

Figure 5.4: (a) depicts the arrowhead travelling wave solution computed for two-dimensional pipe flow at Re = 300, E = 0.6. Coherent flow structures resembling the arrowhead are readily observed across a wide parameter range, examples are shown for (b) $E = 0.55$, $Re = 900$, (c) $E = 0.35$, $Re = 65$, (d)$E = 170$, $Re = 5$. Panel (e) shows a typical measurement carried out across a longer time span, illustrating the dominance and persistence of arrowhead type structures $E = 0.15$ throughout the turbulent dynamics, $Re = 1540$ (same colorbar as previous panels). In all panels the streamwise velocity fluctuations are normalised with the respective bulk velocity. The experimental flow fields ((b)-(e)) are reconstructed by use of the Taylor frozen turbulence hypothesis. for panel (b), E = 0.0055 (shear dependent) and Re = 850 (near onset), because panel c is for 50ppm with 50 % glycerol in 4mm pipe, here the E value is 0.35 (shear dependent), it is not possible that for 100ppm in 20mm pipe, E value is 0.55, and the last panel for 200ppm in 20 mm pipe, E = 0.015, Re = 1540 far from onset

Overall, our observations hence demonstrate that the onset of EIT is neither caused by the proposed TS wave scenario, nor by the hoop stress instability but instead corresponds to the subcritical centre mode instability. The ease of observation and high recurrence rate of coherent flow structures in our experiments, make EIT a promising target for low dimensional dynamical system models.

CHAPTER 6

Discussions and future directions

In this thesis I've shown some of the most interesting flow dynamics corresponding to EIT and MDR at various flow rates. The study of polymer turbulence took root in the beginning mainly focused on the phenomenon of drag reduction, and research in this topic had streamlined itself in this direction, under the assumption that MDR is a marginal form of Newtonian turbulence. The early theories from Virk, de Gennes, and Lumley have regarded the mechanics of drag reduction through the lens of Newtonian turbulence, and has caused the early research from structural turbulence to have glossed over when considering polymeric flows.

We have had major breakthroughs in the last two decades in the realm of viscoelastic instabilities at low inertia, with Elastic turbulence being discovered, and also the discovery of EIT, and naturally this has led to the questions about the relationship these flows have to MDR. In this thesis I have tried to answer some of these questions, and demistify the flow dynamics at various flow parameters.

We have carried out experimental measurements and have the first three dimensionally resolved velocity fields along with pressure and LDV measurements for a variety of these control parameters.

We have been able to visualise the so called arrowhead structures very clearly in our experiments. Although for a 100ppm run these structures begin appearing at $Re\ 900$, we see them persistently, even though the flow dynamics do get more chaotic with increasing Re. Increasing the polymer concentration increases the Elasticity, while decreasing the β, and this only leads the arrowhead structures to become more persistent, and we see a train of arrohead structures in the flow.

Further increase in Re keeping the polymer concentration constant eventually causes the centre mode arrowhead structures to transition to the wall mode. We have found a novel way to visualise and identify different flow states, and that's by visualising the streamwise vorticity, which ends up showing alternating elongated sheets of vorticity, spread azimuthally and layered on top of each other. Such structures are absent in Newtonian flow, but persistent across all the ranges of flow at EIT and MDR that we have observed. Surprisingly such structures are also present right from the formation of the arrowhead structures. Also is interesting is how these structures look identical starting from the wall mode all the way to MDR, indicating a deep relationship between the two states.

The topological structures of Q further span this point. For the first time in experiments I show the spanwise structures of the Q-value, which have been predicted by numerical simulations. These structures persist all the way from the wall mode at low Re, all the way to MDR flow, indicating that the flow at MDR is identical to the flow at wall mode of EIT at low Re. This shows that the flow at MDR is dominated by EIT effects, and not by marginal dynamics of Newtonian turbulence, as many studies in the past have assumed. We also find the energy spectra to follow a -3 curve, for flows covering almost four decades of Re, showing the persisting dynamics of EIT at high Re.

More experiments have been done by changing the concentration of polymers while staying on MDR, and with increasing elasticity, we find that the EIT like structures only gain in prominence.

Experiments have been also done going from Newtonian turbulence to flow at MDR keeping the Re fixed, along what is called the LDR to HDR transition. We find that the drop in friction factors occurs across a very small change in polymer concentrations, compared to the range of polymer concentrations I have tested. This sudden shift in dynamics first comes in the form of the velocity structures changing from NT-like dynamics to more EIT dominated dynamics, with the EIT associated long velocity streaks appearing in the higher drag reducing regimes. What is more interesting is that even though the vorticity structures slowly take the EIT like shape as one approaches MDR, only upon reaching MDR do these structures look EIT-identical.

Bibliography

[ABH23] Marc Avila, Dwight Barkley, and Björn Hof. Transition to turbulence in pipe flow. *Annual Review of Fluid Mechanics*, 55(1):575–602, 2023.

[ACE$^+$87] Ditza Auerbach, Predrag Cvitanović, Jean-Pierre Eckmann, Gemunu Gunaratne, and Itamar Procaccia. Exploring chaotic motion through periodic orbits. *Physical Review Letters*, 58(23):2387, 1987.

[AY86] RJ Adrian and CS Yao. Power spectra of fluid velocities measured by laser doppler velocimetry. *Experiments in Fluids*, 5(1):17–28, 1986.

[Bat00] George Keith Batchelor. *An introduction to fluid dynamics*. Cambridge university press, 2000.

[BMW$^+$03] Volfango Bertola, Bernard Meulenbroek, Christian Wagner, Cornelis Storm, Alexander Morozov, Wim van Saarloos, and Daniel Bonn. Experimental evidence for an intrinsic route to polymer melt fracture phenomena: a nonlinear instability of viscoelastic poiseuille flow. *Physical review letters*, 90(11):114502, 2003.

[BMWH20] Nazmi Burak Budanur, Elena Marensi, Ashley P Willis, and Björn Hof. Upper edge of chaos and the energetics of transition in pipe flow. *Physical Review Fluids*, 5(2):023903, 2020.

[BPK22] Gergely Buza, Jacob Page, and Rich R. Kerswell. Weakly nonlinear analysis of the viscoelastic instability in channel flow for finite and vanishing Reynolds numbers. *Journal of Fluid Mechanics*, 940:A11, 2022.

[BV17] Melissa C Brindise and Pavlos P Vlachos. Proper orthogonal decomposition truncation method for data denoising and order reduction. *Experiments in Fluids*, 58:1–18, 2017.

[CLH18a] George H. Choueiri, Jose M. Lopez, and Björn Hof. Exceeding the asymptotic limit of polymer drag reduction. *Phys. Rev. Lett.*, 120:124501, 2018.

[CLH18b] George H Choueiri, Jose M Lopez, and Björn Hof. Exceeding the asymptotic limit of polymer drag reduction. *Physical review letters*, 120(12):124501, 2018.

[CLV^{+}21] George H. Choueiri, Jose M. Lopez, Atul Varshney, Sarath Sankar, and Björn Hof. Experimental observation of the origin and structure of elastoinertial turbulence. *Proceedings of the National Academy of Sciences*, 118(45):e2102350118, 2021.

[CPST^{+}22] Christopher J Crowley, Joshua L Pughe-Sanford, Wesley Toler, Michael C Krygier, Roman O Grigoriev, and Michael F Schatz. Turbulence tracks recurrent solutions. *Proceedings of the National Academy of Sciences*, 119(34):e2120665119, 2022.

[CSD18] Bidhan Chandra, V Shankar, and Debopam Das. Onset of transition in the flow of polymer solutions through microtubes. *Journal of Fluid Mechanics*, 844:1052–1083, 2018.

[CSD20] Bidhan Chandra, V. Shankar, and Debopam Das. Early transition, relaminarization and drag reduction in the flow of polymer solutions through microtubes. *Journal of Fluid Mechanics*, 885:A47, 2020.

[DG86] PG De Gennes. Towards a scaling theory of drag reduction. *Physica A: Statistical Mechanics and its Applications*, 140(1-2):9–25, 1986.

[DKN98] Adrianus Antonius Draad, GDC Kuiken, and FTM Nieuwstadt. Laminar–turbulent transition in pipe flow for newtonian and non-newtonian fluids. *Journal of Fluid Mechanics*, 377:267–312, 1998.

[DKN18] Nils Damaschke, Volker Kühn, and Holger Nobach. A fair review of non-parametric bias-free autocorrelation and spectral methods for randomly sampled data in laser doppler velocimetry. *Digital Signal Processing*, 76:22–33, 2018.

[DLMAH12] Alberto De Lozar, Fernando Mellibovsky, Marc Avila, and Björn Hof. Edge state in pipe flow experiments. *Physical review letters*, 108(21):214502, 2012.

[DM59] DW Dodge and AB Metzner. Turbulent flow of non-newtonian systems. *AIChE journal*, 5(2):189–204, 1959.

[DPK+22] Yves Dubief, Jacob Page, Rich R Kerswell, Vincent E Terrapon, and Victor Steinberg. First coherent structure in elasto-inertial turbulence. *Physical Review Fluids*, 7(7):073301, 2022.

[DTH23] Yves Dubief, Vincent E Terrapon, and Björn Hof. Elasto-inertial turbulence. *Annual Review of Fluid Mechanics*, 55(1):675–705, 2023.

[DTS13] Yves Dubief, Vincent E Terrapon, and Julio Soria. On the mechanism of elasto-inertial turbulence. *Physics of Fluids*, 25(11):110817, 2013.

[ESHW07] Bruno Eckhardt, Tobias M. Schneider, Bjorn Hof, and Jerry Westerweel. Turbulence Transition in Pipe Flow. *Annual Review of Fluid Mechanics*, 39(1):447–468, 2007.

[FL03] A Fouxon and V Lebedev. Spectra of turbulence in dilute polymer solutions. *Physics of Fluids*, 15(7):2060–2072, 2003.

[GCK+18] Piyush Garg, Indresh Chaudhary, Mohammad Khalid, V Shankar, and Ganesh Subramanian. Viscoelastic pipe flow is linearly unstable. *Physical review letters*, 121(2):024502, 2018.

[GF21] Michael D. Graham and Daniel Floryan. Exact Coherent States and the Nonlinear Dynamics of Wall-Bounded Turbulent Flows. *Annual Review of Fluid Mechanics*, 53:227–253, 2021.

[GS00] Alexander Groisman and Victor Steinberg. Elastic turbulence in a polymer solution flow. *Nature*, 405(6782):53, 2000.

[GS01] Alexander Groisman and Victor Steinberg. Efficient mixing at low reynolds numbers using polymer additives. *Nature*, 410(6831):905–908, 2001.

[HDLKW08] Björn Hof, Alberto De Lozar, Dirk Jan Kuik, and Jerry Westerweel. Repeller or attractor? selecting the dynamical model for the onset of turbulence in pipe flow. *Physical review letters*, 101(21):214501, 2008.

[HGZ19] Ismail Hameduddin, Dennice F Gayme, and Tamer A Zaki. Perturbative expansions of the conformation tensor in viscoelastic flows. *Journal of Fluid Mechanics*, 858:377–406, 2019.

[HMZG18] Ismail Hameduddin, Charles Meneveau, Tamer A Zaki, and Dennice F Gayme. Geometric decomposition of the conformation tensor in viscoelastic turbulence. *Journal of Fluid Mechanics*, 842:395–427, 2018.

[HVDW$^+$04] Bjorn Hof, Casimir WH Van Doorne, Jerry Westerweel, Frans TM Nieuwstadt, Holger Faisst, Bruno Eckhardt, Hakan Wedin, Richard R Kerswell, and Fabian Waleffe. Experimental observation of nonlinear traveling waves in turbulent pipe flow. *Science*, 305(5690):1594–1598, 2004.

[HWM88] Julian CR Hunt, Alan A Wray, and Parviz Moin. Eddies, streams, and convergence zones in turbulent flows. *Studying turbulence using numerical simulation databases, 2. Proceedings of the 1988 summer program*, 1988.

[KCG$^+$21] Mohammad Khalid, Indresh Chaudhary, Piyush Garg, V Shankar, and Ganesh Subramanian. The centre-mode instability of viscoelastic plane poiseuille flow. *Journal of Fluid Mechanics*, 915:A43, 2021.

[Ker05] RR Kerswell. Recent progress in understanding the transition to turbulence in a pipe. *Nonlinearity*, 18(6):R17, 2005.

[KSS21] Mohammad Khalid, V Shankar, and Ganesh Subramanian. Continuous pathway between the elasto-inertial and elastic turbulent states in viscoelastic channel flow. *Physical Review Letters*, 127(13):134502, 2021.

[KUVV12] Genta Kawahara, Markus Uhlmann, and Lennaert Van Veen. The significance of simple invariant solutions in turbulent flows. *Annual Review of Fluid Mechanics*, 44:203–225, 2012.

[LCH19] Jose M. Lopez, George H. Choueiri, and Björn Hof. Dynamics of viscoelastic pipe flow at low reynolds numbers in the maximum drag reduction limit. *Journal of Fluid Mechanics*, 874:699–719, 2019.

[LJS09] Yonggang Liu, Yonggun Jun, and Victor Steinberg. Concentration dependence of the longest relaxation times of dilute and semidilute polymer solutions. *Journal of Rheology*, 53(5):1069–1085, 2009.

[LLM24] Martin Lellep, Moritz Linkmann, and Alexander Morozov. Purely elastic turbulence in pressure-driven channel flows. *Proceedings of the National Academy of Sciences*, 121(9):e2318851121, 2024.

[LSM90] R G Larson, E S G Shaqfeh, and S J Muller. A purely elastic instability in Taylor-Couette flow. *Journal of Fluid Mechanics*, 218:573–600, 1990.

[Lum69] John L Lumley. Drag reduction by additives. *Annual review of fluid mechanics*, 1, 1969.

[LW70] RC Little and M Wiegard. Drag reduction and structural turbulence in flowing polyox solutions. *Journal of Applied Polymer Science*, 14(2):409–419, 1970.

[Moo44] Lewis F Moody. Friction factors for pipe flow. *Transactions of the American Society of mechanical engineers*, 66(8):671–678, 1944.

[Mor22] Alexander Morozov. Coherent structures in plane channel flow of dilute polymer solutions with vanishing inertia. *Physical Review Letters*, 129(1):017801, 2022.

[MPÖ96] Gareth H McKinley, Peyman Pakdel, and Alparslan Öztekin. Rheological and geometric scaling of purely elastic flow instabilities. *Journal of Non-Newtonian Fluid Mechanics*, 67:19–47, 1996.

[MR55] AB Metzner and JC Reed. Flow of non-newtonian fluids—correlation of the laminar, transition, and turbulent-flow regions. *Aiche journal*, 1(4):434–440, 1955.

[MvS05] Alexander N Morozov and Wim van Saarloos. Subcritical finite-amplitude solutions for plane couette flow of viscoelastic fluids. *Physical review letters*, 95(2):024501, 2005.

[MvS19] Alexander Morozov and Wim van Saarloos. Subcritical instabilities in plane poiseuille flow of an oldroyd-b fluid. *Journal of Statistical Physics*, 175(3):554–577, May 2019.

[NDN18] V. Kühn N. Damaschke and H. Nobach. A direct spectral estimation method for laser doppler data using quantization of arrival times. *Proc. of the 19th International Symposium on the Application of Laser and Imaging Techniques to Fluid Mechanics*, 2018.

[OA26] Wo. Ostwald and R. Auerbach. Ueber die Viskosität kolloider Lösungen im Struktur-, Laminar- und Turbulenzgebiet. *Kolloid-Zeitschrift*, 38(3):261–280, 1926.

[PDK20] Jacob Page, Yves Dubief, and Rich R Kerswell. Exact traveling wave solutions in viscoelastic channel flow. *Physical Review Letters*, 125(15):154501, 2020.

[PLB08] Itamar Procaccia, Victor S. L'vov, and Roberto Benzi. Colloquium: Theory of drag reduction by polymers in wall-bounded turbulence. *Rev. Mod. Phys.*, 80:225–247, Jan 2008.

[PMWA13] L. Pan, A. Morozov, C. Wagner, and P. E. Arratia. Nonlinear elastic instability in channel flows at low reynolds numbers. *Phys. Rev. Lett.*, 110:174502, Apr 2013.

[PNBK24] Jacob Page, Peter Norgaard, Michael P Brenner, and Rich R Kerswell. Recurrent flow patterns as a basis for two-dimensional turbulence: Predicting statistics from structures. *Proceedings of the National Academy of Sciences*, 121(23):e2320007121, 2024.

[PW90] FT Pinho and JH Whitelaw. Flow of non-newtonian fluids in a pipe. *Journal of non-newtonian fluid mechanics*, 34(2):129–144, 1990.

[PYD$^+$23] Chaitanya S Paranjape, Gökhan Yalnız, Yohann Duguet, Nazmi Burak Budanur, and Björn Hof. Direct path from turbulence to time-periodic solutions. *Physical Review Letters*, 131(3):034002, 2023.

[QSHA19] Boyang Qin, Paul F. Salipante, Steven D. Hudson, and Paulo E. Arratia. Flow resistance and structures in viscoelastic channel flows at low re. *Phys. Rev. Lett.*, 123:194501, Nov 2019.

[Rei26] Markus Reiner. Zur Theorie der "Strukturturbulenz". *Kolloid-Zeitschrift*, 39(4):314–315, 1926.

[Rey83] Osborne Reynolds. Xxix. an experimental investigation of the circumstances which determine whether the motion of water shall be direct or sinuous, and of the law of resistance in parallel channels. *Philosophical Transactions of the Royal society of London*, (174):935–982, 1883.

[Rot90] Nikolaus Rott. Note on the history of the reynolds number. *Annual review of fluid mechanics*, 22(1):1–12, 1990.

[RT64] A. Ram and A. Tamir. Structural turbulence in polymer solutions. *Journal of Applied Polymer Science*, 8(6):2751–2762, 1964.

[RWS+18] Markus Raffel, Christian E Willert, Fulvio Scarano, Christian J Kähler, Steve T Wereley, and Jürgen Kompenhans. *Particle image velocimetry: a practical guide*. springer, 2018.

[SDH+13] Devranjan Samanta, Yves Dubief, Markus Holzner, Christof Schäfer, Alexander N Morozov, Christian Wagner, and Björn Hof. Elasto-inertial turbulence. *Proceedings of the National Academy of Sciences*, 110(26):10557–10562, 2013.

[Sha96] E.S.G. Shaqfeh. Purely elastic instabilities in viscometric flows. *Ann. Rev. Fluid Mech.*, 28:129–185, 1996.

[SMMG20] Ashwin Shekar, Ryan M McMullen, Beverley J McKeon, and Michael D Graham. Self-sustained elastoinertial tollmien–schlichting waves. *Journal of Fluid Mechanics*, 897:A3, 2020.

[SMMG21] Ashwin Shekar, Ryan M McMullen, Beverley J McKeon, and Michael D Graham. Tollmien-schlichting route to elastoinertial turbulence in channel flow. *Physical Review Fluids*, 6(9):093301, 2021.

[SMW+19] Ashwin Shekar, Ryan M McMullen, Sung-Ning Wang, Beverley J McKeon, and Michael D Graham. Critical-Layer Structures and Mechanisms in Elastoinertial Turbulence. *Physical Review Letters*, 122(12):124503, 2019.

[STD18] Samir Sid, VE Terrapon, and Y Dubief. Two-dimensional dynamics of elasto-inertial turbulence and its role in polymer drag reduction. *Physical Review Fluids*, 3(1):011301, 2018.

[Ste21] Victor Steinberg. Elastic turbulence: an experimental view on inertialess random flow. *Annual Review of Fluid Mechanics*, 53(1):27–58, 2021.

[STGS17] Balachandra Suri, Jeffrey Tithof, Roman O Grigoriev, and Michael F Schatz. Forecasting fluid flows using the geometry of turbulence. *Physical review letters*, 118(11):114501, 2017.

[SW00] Katepalli R Sreenivasan and Christopher M White. The onset of drag reduction by dilute polymer additives, and the maximum drag reduction asymptote. *Journal of Fluid Mechanics*, 409:149–164, 2000.

[TDG86] M Tabor and PG De Gennes. A cascade theory of drag reduction. *Europhysics Letters*, 2(7):519, 1986.

[Tom48] B. A. Toms. Some observation on the flow of linear polymer solutions through straight tubes at large Reynolds numbers. In *Proc. 1st Intl. Congr. on Rheology*, volume Vol. II, pages 135–141, 1948.

[VDW07] CWH Van Doorne and Jerry Westerweel. Measurement of laminar, transitional and turbulent pipe flow using stereoscopic-piv. *Experiments in fluids*, 42:259–279, 2007.

[Vir71] PS Virk. An elastic sublayer model for drag reduction by dilute solutions of linear macromolecules. *Journal of Fluid Mechanics*, 45(3):417–440, 1971.

[VM13] Richard Vonlanthen and Peter A Monkewitz. Grid turbulence in dilute polymer solutions: Peo in water. *Journal of Fluid Mechanics*, 730:76–98, 2013.

[VMS70] P.S. Virk, H.S. Mickley, and K.A. Smith. The ultimate asymptote and mean flow structure in toms' phenomenon. *J. Appl. Mech.*, 37(2):488–493, 1970.

[VSW97] PS Virk, DC Sherman, and DL Wagger. Additive equivalence during turbulent drag reduction. *American Institute of Chemical Engineers. AIChE Journal*, 43(12):3257, 1997.

[WM08] Christopher M. White and M Godfrey Mungal. Mechanics and prediction of turbulent drag reduction with polymer additives. *Annual Review of Fluid Mechanics*, 40(1):235–256, 2008.

[WMH99] MD Warholic, H Massah, and TJ Hanratty. Influence of drag-reducing polymers on turbulence: effects of reynolds number, concentration and mixing. *Experiments in fluids*, 27(5):461–472, 1999.

[WSZ21] Dongdong Wan, Guangrui Sun, and Mengqi Zhang. Subcritical and supercritical bifurcations in axisymmetric viscoelastic pipe flows. *Journal of Fluid Mechanics*, 929:A16, 2021.

[XB16] Li Xi and Xue Bai. Marginal turbulent state of viscoelastic fluids: A polymer drag reduction perspective. *Physical Review E*, 93(4):043118, 2016.

[XG10] Li Xi and Michael D. Graham. Active and hibernating turbulence in minimal channel flow of newtonian and polymeric fluids. *Phys. Rev. Lett.*, 104:218301, May 2010.

[XG12] Li Xi and Michael D. Graham. Dynamics on the laminar-turbulent boundary and the origin of the maximum drag reduction asymptote. *Phys. Rev. Lett.*, 108:028301, 2012.

[YHB21] Gökhan Yalnız, Björn Hof, and Nazmi Burak Budanur. Coarse graining the state space of a turbulent flow using periodic orbits. *Physical Review Letters*, 126(24):244502, 2021.

[YKR$^+$21] Sami Yamani, Bavand Keshavarz, Yashasvi Raj, Tamer A Zaki, Gareth H McKinley, and Irmgard Bischofberger. Spectral universality of elastoinertial turbulence. *Physical Review Letters*, 127(7):074501, 2021.

[ZCW$^+$24] Hongna Zhang, Haotian Cheng, Suming Wang, Wenhua Zhang, Xiaobin Li, and Fengchen Li. The minimal flow unit and origin of two-dimensional elasto-inertial turbulence. *Journal of Fluid Mechanics*, 999:A82, 2024.

[ZGRW10] A. Zell, S. Gier, S. Rafaï, and C. Wagner. Is there a relation between the relaxation time measured in caber experiments and the first normal stress coefficient? *Journal of Non-Newtonian Fluid Mechanics*, 165(19):1265 – 1274, 2010.

[Zim56] Bruno H Zimm. Dynamics of polymer molecules in dilute solution: viscoelasticity, flow birefringence and dielectric loss. *The journal of chemical physics*, 24(2):269–278, 1956.

[ZX20] Lu Zhu and Li Xi. Inertia-driven and elastoinertial viscoelastic turbulent channel flow simulated with a hybrid pseudo-spectral/finite-difference numerical scheme. *Journal of Non-Newtonian Fluid Mechanics*, 286:104410, 2020.

[ZX21] Lu Zhu and Li Xi. Nonasymptotic elastoinertial turbulence for asymptotic drag reduction. *Physical Review Fluids*, 6(1):014601, 2021.

[ZZL$^+$21] Wen-Hua Zhang, Hong-Na Zhang, Yu-Ke Li, Bo Yu, and Feng-Chen Li. Role of elasto-inertial turbulence in viscoelastic drag-reducing turbulence. *Physics of Fluids*, 33(8), 2021.

[ZZW$^+$22] Wen-Hua Zhang, Hong-Na Zhang, Zi-Mu Wang, Yu-Ke Li, Bo Yu, and Feng-Chen Li. Repicturing viscoelastic drag-reducing turbulence by introducing dynamics of elasto-inertial turbulence. *Journal of Fluid Mechanics*, 940:A31, 2022.